On the Nature and Extent of Optically-Thin Marine Low Clouds

L. V. Leahy*, R. Wood, and R. J. Charlson
Department of Atmospheric Sciences, University of Washington, Seattle, Washington, USA

C. A. Hostetler, R. R. Rogers
NASA Langley Research Center, Hampton, VA

M. A. Vaughan, D. M. Winker
NASA Langley Research Center, Hampton, VA

Submission for publication to *Journal of Geophysical Research:*
Corresponding Author*: Louise Leahy
University of Washington
Department of Atmospheric Sciences
Box 351640
Seattle, WA 98195-1640 USA
Tel: (206) 543 4250
Fax: (206) 543 0308
Email:lleahy@atmos.washington.edu

Abstract

Macrophysical properties of optically-thin marine low-clouds over the non-polar oceans (60°S-60°N) are measured using two years of full-resolution nighttime data from the Cloud-Aerosol Lidar with Orthogonal Polarization (CALIOP). Optically-thin clouds, defined as the subset of marine low clouds that do not fully attenuate the lidar signal, comprise almost half of the low-clouds over the marine domain. Regionally, the fraction of low clouds that are optically-thin ($f_{thin,cld}$) exhibits a strong inverse relationship with the low-cloud cover, with maxima in the tropical trades ($f_{thin,cld} > 0.8$) and minima in regions of persistent marine stratocumulus and in midlatitudes ($f_{thin,cld} < 0.3$). Domain-wide, a power law fit describes the cloud length distribution, with exponent $\beta = 2.03 \pm 0.06$ (± 95% confidence interval). On average, the fraction of a cloud that is optically-thin decreases from ~1 for clouds smaller than 2 km, to <0.3 for clouds larger than 30 km. This relationship is found to be independent of region, so that geographical variations in the cloud length distribution explain three-quarters of the variance in $f_{thin,cld}$. Comparing collocated trade cumulus observations from CALIOP and the airborne High Spectral Resolution Lidar reveals that clouds with lengths smaller than are resolvable with CALIOP contribute approximately half of the low clouds in the region sampled. A bounded cascade model is constructed to match the observations from the trades. The model shows that the observed optically-thin cloud behavior is consistent with a power law scaling of cloud optical depth and suggests that most optically-thin clouds only partially fill the CALIOP footprint.

1.0 Introduction

The planetary albedo is a quantity determined by the reflection of sunlight by the Earth's surface and atmosphere. It is a critical determinant of the Earth's temperate and climate, and it is therefore imperative that its controlling factors be understood and adequately quantified. Without clouds, the planetary albedo would be about 0.15, due to the low reflectance of the Earth's surface (most of which is ocean). Highly reflective surfaces, such as those characteristic of the polar regions and unvegetated deserts, are notable exceptions but cover a small part of the planet and do not contribute strongly to the average surface albedo. However, the average albedo of the Earth (~0.3) is roughly doubled by the presence of clouds [*Harrison et al*., 1990], and low clouds are the dominant type by contribution to albedo [*Hartmann et al*., 1992].

Among albedo-influencing components of the Earth system, clouds are unique in both their extreme transience and in their remarkable range of sizes and forms. Although we have a reasonably accurate assessment of the global impact of clouds on the planetary albedo, our understanding of how clouds of different sizes and types contribute to the albedo remains rather poor. Although it is known that low clouds are the dominant contributor to the albedo globally [*Hartmann et al*., 1992], it is uncertain what the relative contributions of the different low cloud types (cumulus, stratocumulus, stratus) are to the overall albedo of low clouds.

Moist convection over the oceans has a varied morphology. Marine low clouds range from expansive stratocumulus decks stretching hundreds of kilometers, to small trade wind cumulus a few tens to hundreds of meters in extent [*Hozumi et al*., 1982; *Wood and Field*, 2011]. We are currently unable to quantify how different low-cloud systems distribute condensate horizontally and vertically to determine their albedo. This is partly because we do not fully understand how albedo scales with cloud cover, as the latter is frequently difficult to measure with the moderate-resolution (~1 km) passive sensors used to generate our cloud cover climatologies [*Zhao and Di Girolamo*, 2006; *Jones et al.,* 2012]. We still do not have proven measures of cloud condensate amounts, particularly for broken and optically-thin cloud fields [*Turner et al*., 2007]. Many questions are therefore still largely unanswered. For example, per unit of cloud cover, are trade cumulus clouds optically thinner than stratocumulus? What fraction of low clouds is optically-thin and how are these optically-thin clouds partitioned by cloud size and type? What resolution do our passive sensors need to have in order to accurately determine cloud cover?

Satellite data show that the albedo of extensive marine low clouds is quite low [*Bender et al*., 2011], and that their optical thickness is highly variable (e.g., *Rossow et al*. [2002]). It is reasonable to infer that a significant fraction of them must be optically-thin. These optically-thin clouds are not currently well resolved observationally, but are globally pervasive and potentially important for climate studies [*Garret and Zhao,* 2006; *Turner et al*., 2007; *Zuidema et al*., 2012]. For this work, we define operationally an optically-thin cloud as a cloud that does not fully attenuate a lidar backscatter signal. This corresponds to unbroken clouds with optical depth (τ_{cld}) less than ~3. Analysis of τ_{cld} from Moderate Resolution Imaging Spectroradiometer (MODIS) Level 3 liquid cloud retrievals over an ocean region spanning (±45° latitude) suggests that clouds with $\tau_{cld} < 3$ comprise ~30% of marine low clouds, and contribute perhaps 15% of their albedo (Fig. 1). But since many of these clouds are known to be smaller than the resolution of the MODIS pixels (e.g., *Zhao and Di Girolamo* [2007]), it is important to appreciate that these estimates are likely to be a function of sensor resolution. How does the picture change when clouds are viewed with an active sensor with a much smaller footprint size? Indeed, does the use of metrics such as

cloud cover even make sense if a significant fraction of the clouds have very low optical thicknesses?

Optically-thin and broken clouds are not only important because of their contribution to the planetary albedo, but also because aerosol retrievals are problematic where clear regions are in close proximity to clouds and contamination of clear pixels by sub-pixel scale optically-thin clouds is common (e.g., *Zhang and Reid* [2005], *Charlson et al.* [2007], *Koren et al.* [2007]). A trade wind cumulus study reported that a third of MODIS pixels diagnosed by the cloud mask as being clear actually contained sub-pixel scale cloud [*Zhao and Di Girolamo,* 2006]. Over the global ice-free oceans, 50% of marine low clouds are separated from each other by less than 5 km [*Várnai and Marshak,* 2011], suggesting that a high fraction of clear sky over ocean is in close proximity to cloud. Other recent studies of the clear-cloud transition region using both *in situ* [*Twohy et al.,* 2009] and remote sensing measurements [*Su et al.,* 2008; *Tackett and Di Girolamo,* 2009; *Redemann et al.,* 2009] suggest that aerosol properties in the vicinity of clouds are different from those 2-5 km from the cloud. Some of this difference may be attributed to aerosol hygroscopic growth in the high relative humidity air surrounding cloud, but the relative magnitudes of cloud contamination and aerosol hygroscopic growth effects on retrieved aerosol properties is not known. Observations show that enhancement of near-cloud reflectances due to undetected or unresolved cloud contamination of clear pixels leads to passive sensor aerosol optical depth retrieval overestimates of 10-20% [*Zhang and Reid,* 2005].

Although passive sensors provide excellent coverage, it is fundamentally challenging to identify which atmospheric constituents are producing the measured top of atmosphere (TOA) signals, and at what altitudes they reside. Spaceborne lidar provides a metric of the TOA reflectance, integrated over the specified layers of interest, and offers a closer link to the atmospheric constituent producing that signal than passive sensors provide. A frequency distribution of such a metric, integrated attenuated backscatter (IABS), derived from high-resolution (90 m telescope footprint) Cloud-Aerosol Lidar with Orthogonal Polarization (CALIOP) is presented in Fig. 2. A bimodal distribution of IABS is observed with modes representing clear and cloudy atmospheric states as indicated (Fig. 2a). The non-zero minimum between clear and cloudy states, which exemplifies the fundamental challenge in separating clouds from clear sky, has been termed the "continuum" region [*Charlson et al.,* 2007]. With detailed classification with CALIOP's full-resolution cloud clearing algorithm [*Vaughan et al.,* 2009]), spaceborne lidar is able to inform us that this "continuum", or clear-cloud transition region, is populated almost exclusively with clouds (Fig. 2b). These clouds must, by their virtue of having low visible reflectance, be optically-thin. IABS can be small either because the cloud is optically-thin or because the laser was attenuated fully some distance into an optically-thick cloud. The latter case is manifest in Fig. 2b as the smaller values of IABS categorized as optically-thick clouds. A frequency distribution alone cannot inform us of their spatial structure, but previous work suggests a prevalence of detraining cloud elements, dissipating, or nascent clouds in marine low-cloud systems [*Koren et al.,* 2009]. However, the CALIOP data are showing us that optically-thin clouds are not only limited to the "continuum" region (approximately defined as the IABS region spanning 5×10^{-2} sr^{-1} to 3×10^{-1} sr^{-1}), but contribute to TOA reflectance throughout the entire cloud IABS distribution (Fig. 2b). Indeed, over non-polar oceans, we find that almost half of the marine low clouds are optically-thin by our definition of surface-detectability.

Despite the apparent prevalence of optically-thin clouds, very little is currently known about their macrophysical properties (spatial distribution, length, vertical

142 distribution, geometric depth) on a global scale. This study aims to provide insight into
143 these properties, and thereby provide new information on a poorly characterized and
144 understood subset of marine low clouds. Compared to satellite observations, large scale
145 models tend to overestimate the frequency of optically-thick low clouds and underestimate
146 the frequency of optically-thin low clouds (e. g., *Kay et al*., [2012] a Community
147 Atmosphere Model study). At the low end of the optical depth distribution, model
148 frequencies are close to an order of magnitude too low compared to passive remote sensing
149 satellite observations [*Kay et al*., 2012]. However, it is important to appreciate that there
150 are major differences between the various observational datasets [see Fig. 3 in *Kay et al*.,
151 2012], making accurate assessment of model representation of optically-thin low clouds
152 difficult.
153 The primary dataset employed for this study is the CALIOP full-resolution cloud
154 mask (60 m vertical resolution and 90 m footprint diameter, spatially sampled every 335 m)
155 at 1064 nm. In addition to providing new near-global observations of the macrophysical
156 properties of optically-thin marine low clouds, we also investigate possible sensor-
157 resolution detection issues by comparing CALIOP with data from NASA's airborne High
158 Spectral Resolution Lidar (HSRL). The ensuing sections of this manuscript are ordered as
159 follows. Dataset description and analysis methodology are detailed in Section 2. Results
160 are presented in Section 3. A discussion of the implications is augmented and informed by
161 the use of a simple fractal model in Section 4. Our findings are summarized in Section 5.
162
163

2.0 Dataset Description and Analysis Method

2.1 CALIOP Dataset

Two years (September 2006-August 2008) of vertically-resolved cloud data from the full-resolution CALIOP Vertical Feature Mask (VFM) Version 3.01 [*Vaughan et al.,* 2009] over the non-polar oceans (±60° latitude) are used in this study. The VFM provides vertically-resolved cloud and aerosol layer information generated by the CALIOP multi-resolution layer identification and scene classification algorithms. Full-resolution layer information is obtained from the high-resolution cloud clearing tool within the layer detection algorithm. In the lowest 4 km of the atmosphere the 1064 nm channel (60 m vertical resolution) is used for full-resolution cloud-layer identification, and any feature detected above the surface is classified as a cloud [*Vaughan et. al.,* 2009]. This wavelength is less sensitive to aerosol than the 532 nm channel and this improves cloud-aerosol discrimination. A detailed mission overview and comprehensive instrument details are presented by *Winker et al.* [2009] and *Hunt et al.* [2009], respectively. CALIOP has high sensitivity at low cloud optical depths: nighttime minimum detectable particulate extinction at 1064 nm is 0.165 km^{-1} for layers greater than 180 m in depth, equivalent to τ_{cld} greater than 0.03, and is 1.65 km^{-1} for layers 60-180 m (minimum 60 m), equivalent to τ_{cld} greater than 0.1 (Chepfer, H., G. Cesana, D. Winker, B. Getzewich, and M. Vaughan, Comparison of two different cloud climatologies derived from CALIOP-Level 1 observations: the CALIPSO-ST and the CALIPSO-GOCCP, submitted to *Journal of Atmospheric and Oceanic Technology*, 2012). CALIOP provides near-global (± 82° latitude), vertically-resolved, atmosphere-only backscatter data, with no contamination from surface return or 3-D radiation/cloud adjacency effects, unlike radiances measured from passive sensors [*Wen et al.,* 2007; *Várnai and Marshak*, 2009]. However, sampling is sparse. The lidar return signal is limited to a 90 m diameter receiver footprint, so no off-track atmospheric information can be provided. Results are only representative of a single sampling time for every location. In addition, consecutive laser footprints are not contiguous; horizontal separation between each footprint is 335 m and consecutive nighttime (and daytime) orbits are ~2,600 km apart at the Equator, requiring a temporally extensive dataset for representative sampling.

Our focus is optically-thin marine low clouds. In this study, a low cloud is defined as having a cloud top height (CTH) less than or equal to 3 km. A high cloud is any cloud higher than this. We define an optically-thin cloud as a cloud detected at full-resolution that does not fully attenuate the lidar signal (i.e., one for which the ocean surface was also detected in the same profile), corresponding to τ_{cld} less than or equal to 3. Optically-thick clouds are all other low cloud not classified as optically-thin. We screen the data for both high clouds, and incidences of low clouds where more than one cloud-layer is detected, the latter representing a small fraction of the marine low cloud data, 0.06 on average. To ensure the highest fidelity in our results, we use only nighttime data for optimal detection of optically-thin clouds; the solar background signal degrades the daytime signal-to-noise ratio (SNR) [*Hunt et al.,* 2009]. The daytime minimum detectable particulate extinction at 1064 nm is 0.28 km^{-1}, equivalent to τ_{cld} greater than 0.05 for layers greater than 180 m in depth and is 2.8 km^{-1} for layers 60-180 m in depth, equivalent to τ_{cld} greater than 0.17. Inspection of daytime IABS distributions does not reveal large differences between daytime and nighttime data, but it is not possible to separate real diurnal differences from potential differences in detectability and other noise-related artifacts. We note that some aerosol layers (e.g., Saharan dust) may be dense enough to be misclassifiied as cloud at full-resolution, however, this occurs mostly over land and we assume the effects over ocean to

be negligible. In this work a profile is defined as a column of vertically-resolved VFM clear or cloud classifications derived from a single lidar pulse. We further define a cloudy profile as a full-resolution profile with one or more 60 m vertically-adjacent cloud layers. Multi-layered low clouds, comprising less than 6% of the high-cloud screened low cloud dataset, are excluded from this analysis. In summary, our primary dataset is comprised of clear profiles and single-layer cloudy profiles with CTH less than or equal to 3 km detected at full-resolution at night over non-polar oceans.

To provide an example of optically-thin clouds and their spatial context, we present collocated Wide Field Camera (WFC) band-averaged radiance (620 – 670 nm) for a 10 km orbit segment at 125 m horizontal resolution, and CALIOP full-resolution Level 1 daytime IABS at 532 nm integrated from 0 to 20 km, for a broken cloud field in the northwest subtropical Atlantic (Fig. 3). Along with CALIOP, the WFC is part of the Cloud Aerosol Lidar with Integrated Pathfinder Satellite Observation (CALIPSO) satellite's payload. The WFC context (Fig. 3a) suggests that some detected optically-thin cloud profiles are cloud edges that partially fill the lidar field of view. We explore this issue further in Section 4. In general, peaks and troughs observed in both the radiance and IABS data track each other remarkably well (Fig. 3b). Optically-thick cloud profiles (fully attenuated profiles) tend to be associated with stronger visible radiances. However, radiances associated with optically-thick clouds at ~6 km along the orbit segment are similar to some of the radiances for optically-thin cloud profiles elsewhere. The lack of a complete correspondence between radiance and IABS is indicative of the different nature of the lidar backscatter signal and the visible reflectance. Multiple scattering affects the signals in different ways. In addition, it is likely that beam filling in this broken cloud field affects visible radiance and lidar signals differently. The clear evidence in this example for small and often optically-thin cloud elements on the scale of the lidar footprint compels us to understand how optically-thin clouds are related to cloud horizontal scales globally and regionally.

2.2 HSRL Dataset

In addition to a near-global examination of CALIOP's view of optically-thin marine low clouds, we also compare collocated CALIOP cloud fractions and cloud lengths with those estimated using the airborne NASA LaRC High Spectral Resolution Lidar (HSRL) [*Hair et al.,* 2008]. Although HSRL is typically employed for aerosol studies and/or instrument validation (e.g., *Kacenelenbogen et al.* [2011], *Rogers et al.* [2011]) for this work we use derived HSRL altitudes of the ocean surface and cloud top. Cloud data for the comparison are drawn from four daytime and four nighttime spatially and temporally matched HSRL underflights of the CALIOP orbit track over the tropical and subtropical western Atlantic (Table 1), and we include only data for flight segments with aircraft altitude greater than 8 km. HSRL cloud screening is based upon a wavelet transform technique [*Su et al.,* 2008]. HSRL and CALIOP do not have the same footprint dimensions due to different sampling configurations. The HSRL sample area is composed of 60 m along-track averages of contiguous 8 m single-shot footprints, yielding a sample area 8 mx60 m in the across-track and along-track directions, respectively. The 60 m along-track dimension results from 2 Hz sampling at aircraft ground-speed of 120 m s^{-1} (mean value for data analyzed herein). However, CALIOP 90 m diameter footprints are horizontally separated by 335 m in the along-track direction. Henceforth, we refer to an instrument footprint, pixel size or sample area as a field of view (FOV) for clarity of notation. HSRL data have 30 m vertical resolution. In keeping with the CALIOP analysis, we identify cloudy HSRL profiles as those with CTH less than or equal to 3 km. We use

the HSRL ocean surface altitude parameter to determine whether a surface return was detected and thereby discriminate between low and high optical depth clouds, i.e., whether or not the signal was fully-attenuated by the cloud before reaching the surface. For the ocean data used, we expect the surface altitude for a cloud profile to be ~ 0 m if the signal is not fully attenuated. However, the surface altitude detection algorithm is not fully developed (HSRL Data Summary, unpublished material, 2009) and the detected surface altitude departs somewhat from zero, even for cloud-free profiles over the ocean. Therefore, we define a cloud profile with surface altitude less than or equal to 85 m as optically-thin. The upper limit of 85 m is the mean surface altitude plus three standard deviations observed for cloud-free HSRL profiles over the ocean. For the HSRL-CALIOP comparisons, we include only HSRL and CALIOP data that achieve temporal coincidence within ±15 minutes. Both datasets are high-cloud-screened using the CALIPSO VFM described in Section 2.1

2.3 Analysis Methods

After screening for high cloud, CALIOP full-resolution data are binned into 5°x5° latitude-longitude gridboxes. Gridding the data allows us to examine the geographical variations of the various cloud features observed. We define a transect as being the portion of ground track for each CALIPSO orbit within a gridbox. Separate analysis methods are applied to these binned data to produce cloud cover statistics, and cloud length distributions.

2.3.1 Cloud Cover Analysis Method

Monthly cloud cover values calculated from counts of full-resolution clear profiles and low-cloud profiles within a gridbox (Table 2) are averaged to produce two-year mean low-cloud cover values for each gridbox. Domain-wide cloud cover is the mean of all gridbox values.

Minima in high-cloud-screened CALIOP profile counts (Fig. 4a) exhibit a similar pattern to ISCCP – D2 cloud amount maxima for mid plus high clouds (available from http://isccp.giss.nasa.gov/products/browsed2.html). ISCCP annual mean data (not shown) indicate maximum high cloud amounts in the western equatorial Pacific and northern Indian Ocean (amounts > 40%), and mid-level cloud amount maxima (30-40%) in the Northern and Southern Hemisphere storm-track regions.

2.3.2 Cloud Length Distribution Method

Cloud length is calculated for individual cloud entities. We define a cloud entity as a series of consecutive marine low-cloud profiles, bounded on each end by a clear profile. The cloud length data are binned into logarithmically spaced size bins, with the lower size limit set by instrument resolution, and the upper limit defined by the sampling method discussed below. An additional criterion is applied to the size distribution data that is not required for cloud cover analysis: we require a transect to comprise at least 100 km of consecutive high-cloud-screened profiles, thus ensuring a long enough transect length to capture most of the contributions to cloud cover from clouds of different sizes. A transect may be less than 100 km, and therefore excluded from the cloud length dataset, because a) it "clips" the edge of a 5°x5° gridbox, b) high cloud screening eliminates a portion of the transect so that the remaining segment lengths are shorter than 100 km, or c) a portion of transect is land. However, even transects longer than 100 km have a maximum length (~550 km) imposed by the 5°x5° gridding. For every cloud length calculated we retain the length of the transect containing the observed cloud, and use this information to formulate a

simple correction to the size distribution (see *Wood and Field* [2011] for details) to account for this upper limit cut-off as follows,

$$n_{corr}(L)dL = n(L)dL[L_{tran}/(L_{tran} - L_{min})] \quad (1)$$

where $n_{corr}(L)$ is the corrected cloud count, L_{tran} is the mean of the binned transect lengths, L_{min} is the bin minimum cloud length, $n(L)\,dL$ is the number of clouds sampled with sizes between L and $L + dL$. To help elucidate the contributions of optically-thin and optically-thick profiles to clouds of a given size, we construct size distributions for "majority optically-thick" entities (contiguous cloudy profiles for which over 90% of contributing profiles are optically-thick) and "majority optically-thin" entities (over 90% of contributing profiles are optically-thin). The threshold of 90% was chosen to accommodate observed variability in cloud optical depth [*Wood and Taylor,* 2002*; Rossow et al.,* 2002], while ensuring that the clouds analyzed were predominantly optically thick or optically thin, respectively. The cloud length dataset is a subset of the dataset described in Section 2.3.1, and is comprised of approximately three times fewer profiles (cf. Fig. 4a and 4b) because of the minimum transect length restriction.

3.0 Results

3.1 Cloud Cover

High-cloud-screened marine low-cloud cover (f_{cld}) is at a minimum throughout the deep tropics, and is at a maximum in the northern hemisphere and southern hemisphere storm-track regions, with additional maxima in the stratocumulus regions on the eastern side of the oceanic subtropical highs (Fig. 5a). Values range from 0.10 to greater than 0.80, with a two-year, domain mean of 0.50. The spatial pattern of cloud cover is similar to climatologies from surface observations (Warren et al., 2010, Climatic atlas of clouds over land and ocean, available from *http://www.atmos.washington.edu/CloudMap*) and remote sensing [*Rossow and Schiffer,* 1999]. Optically-thin low clouds are present in 10-30% of high-cloud-screened profiles over the non-polar oceans, with no strong geographic variation (f_{thin}; Fig. 5b). When expressed as the fraction of marine low-cloud profiles that are optically-thin ($f_{thin,cld}$), a clear spatial pattern emerges, with maxima in the trade wind cumulus regions, and minima in persistent stratocumulus and storm-track regions (Fig. 5c). The two-year mean value of $f_{thin,cld}$ is 0.45 demonstrating that almost half of all marine low clouds are optically thin. While 0.45 is higher than that from MODIS (Fig. 1), both sensors indicate a major role for optically-thin clouds in determining global cloud cover.

A remarkably strong negative correlation between $f_{thin,cld}$ and f_{cld} exists at both monthly and annual timescales (Fig. 6). In the trade wind regions, where marine low-cloud cover is lower than 0.25 [Fig. 5a, and *Medeiros et al.,* 2010], it is remarkable that consistently greater than 80% of the observed clouds are optically thin. In regions typical of marine stratocumulus, where nighttime marine low-cloud cover exceeds 0.80, $f_{thin,cld}$ is consistently lower, with values of 0.30 or less being typical. The presence of a large amount of marine low cloud that is optically-thin on the scale of the relatively small CALIOP footprint is surprising and warrants further investigation. We devote much of this paper to analyzing these optically-thin clouds. However, we should note that this result is consistent with the TOA albedo from Clouds and the Earth's Radiant Energy System (CERES) data (available from *http://eos.atmos.washington.edu/cgi-bin/ceres/disp.pl?ceres.alb.ann.d)* of the trade wind regions being quite low (typically 0.16) despite cloud coverage in the trade wind regions of 0.20–0.25. Given observed trade wind TOA albedo and cloud cover, and using a simple cloud albedo – cloud optical depth relation [*Lacis and Hansen,* 1974] and a simple TOA albedo model (see Section 4), we estimate that cloud optical depth τ_{cld} would need to be 2.7–3.0 to produce the observed TOA albedo, if all clouds have the same τ_{cld}. While the prevalence of optically-thin clouds may appear surprising, it is consistent with regional albedo observations.

3.2 Cloud Length Distribution

Here, we examine the properties of marine low clouds, and especially optically-thin clouds, as a function of their horizontal scale. Results presented in this section are derived from analysis of cloud entities. We find that cloud length distributions approximately follow a power law fit ($n(L) = \alpha L^{-\beta}$), where n(L) is the number of clouds of size L to L+dL, L is the bin center, and α and β are constants, consistent with previous studies [*Zhao and Di Girolamo*, 2007; *Wood and Field*, 2011; *Benner and Curry*, 1998]. For $\beta = 2$, each logarithmic size interval (e.g., 100m-1km, 1km-10km, etc.) contributes equally to total cloud cover and $\beta > (<) 2$ implies that the distribution is weighted towards smaller (larger) clouds [*Wood and Field,* 2011].

For the CALIOP dataset comprising all low clouds, the size distribution is well fitted by a single power law with $\beta = 2.03 \pm 0.06$ (error at 2σ level). This is higher than the value

of 1.66±0.04 reported by *Wood and Field* [2011] for a near-global cloud dataset comprising aircraft and satellite data. One explanation may be differences in cloud sampling at the low and high ends of the size distribution. Although *Wood and Field* [2011] aircraft data have a higher resolution than CALIOP, ~100 m compared to 335 m, respectively, the aircraft did not sample regions where small cumulus is the dominant cloud type [*Wood and Field*, 2000, 2011]. Further, CALIOP may undersample large clouds as the upper cloud length limit for this study is ~550 km compared to ~4000 km in *Wood and Field* [2011]. Thus, our dataset tends to sample smaller clouds on average, and smaller clouds tend to have larger exponents (see below, and Fig. 12 in *Wood and Field* [2011]).

"Majority optically-thin" clouds (defined in Section 2.3.2) constitute nearly all of the clouds smaller than 4 km, whereas clouds larger than 35 km have a greater contribution from optically-thick profiles (Fig. 7). This highlights the increasing importance of optically-thin clouds as clouds become smaller.

To further explore differences in cloud length distributions, we focus on three specific cloud regimes (Table 3): 1) a region of persistent stratocumulus off the California coast; 2) a tropical Pacific stratocumulus to cumulus (Sc-Cu) transition region; 3) a trade wind cumulus region of the tropical Pacific. Cloud length distributions for the regions of stratocumulus and Sc-Cu transition follow a $\beta < 2$ power law fit with values of 1.81±0.08 and 1.68±0.09, respectively, indicating that large clouds dominate cloud cover (Fig. 7, inset). As expected, the trade wind cloud length distribution has a β greater than 2 (2.49±0.25) and is dominated by clouds with lengths less than 2 km, consistent with prior studies of trade wind cumulus [*Benner and Curry,* 1998; *Zhao and Di Girolamo,* 2007]. Since trade wind regions consist largely of optically-thin clouds (Fig. 5c), these results paint an emerging picture of small marine low clouds being optically-thin. This has implications for the remote sensing of cloud and aerosol properties given current sensor resolution for most passive satellite instruments used to construct cloud climatologies.

3.2.1 Cloud Length at Median Cloud Cover

We define a cloud length at median cloud cover (L_{50}) for each of the three cloud categories (marine low cloud, "majority optically-thin" cloud, "majority optically-thick" cloud) such that clouds with lengths up to L_{50} contribute 50% to cloud cover for that category. Regions with the smallest coverage of low cloud are associated with smaller L_{50} values (cf. Fig. 5a and Fig. 8a), with $L_{50} < 2$ km in trade wind cumulus regions and $L_{50} > 30$ km in stratocumulus regions. Our results for the trades are qualitatively consistent with a recent study in the tropical western Atlantic trade wind region reporting L_{50} of 2 km using high-resolution passive visible satellite data [*Zhao and Di Girolamo,* 2007]. Additionally, we observe an inverse relationship between marine low cloud L_{50} and β (not shown) also noted by *Wood and Field,* [2011], indicating that variations in β explain almost one-third of the observed geographical variance in L_{50}. Instances of horizontally extensive (greater than 10 km) "majority optically-thin" clouds are observed (Fig. 7) but with an order of magnitude smaller frequency than "majority optically-thick" clouds at these lengths. Most notably, poleward of 40° in both hemispheres, "majority optically-thin" L_{50} ranges from 5 km to greater than 10 km (Fig. 8b). Cloud cover in these regions is mainly Sc (Warren et al., 2010, Climatic atlas of clouds over land and ocean http://www.atmos.washington.edu/CloudMap/WebO/index.html). These relatively large L_{50} values are consistent with the dimensions of clouds in shallow open cellular convection [*Wood and Hartmann*, 2006]. "Majority optically-thick" and "majority optically-thin" L_{50}

maps support our earlier statement that optically-thin marine low clouds are in general, smaller in size than optically-thick marine low clouds (Fig. 8b and 8c).

3.2.2 Cloud Length Distribution from HSRL

The horizontal separation between consecutive CALIOP pulses is 0.335 km but many small cumuli are only a few tens to hundreds of meters in size [*Plank 1969; Hozumi et al*., 1982*; Wielicki and Welch,* 1986; *Koren et al.,* 2008]. The inter-profile region not sampled by CALIOP may be populated with one or more small clouds with clear gaps, or may be entirely clear. For our cloud length estimates, if two consecutive profiles are flagged as cloudy we assume that the intervening atmosphere is cloudy, and this could lead to CALIOP overestimating cloud lengths. To examine the extent to which this may occur, we compare spatially matched CALIOP and HSRL cloud length data, noting that HSRL footprints are contiguous. Data are from the tropical western Atlantic trade wind region (Section 2.2 for dataset description).

A minimum transect length criterion of 30 km is applied to the HSRL-CALIOP comparison dataset for estimation of cloud lengths. This is shorter than for our analysis from CALIPSO alone (100 km), because the ± 15 minute temporal matching limits transect lengths to less than 200 km, and we find that a minimum length requirement of 100 km greatly reduces the data available for comparison in what is already a relatively small dataset of collocated data. However, this work (Fig. 8) and other studies indicate that characteristic cloud lengths in the tropical western Atlantic region are substantially smaller than 30 km [*Benner and Curry*, 1998; *Wielicki and Welch*, 1986; *Zhao and Di Girolamo,* 2007], and so our reduced transect length threshold for the HSRL/CALIOP size distribution comparison should not produce large problems.

The CALIOP and HSRL cloud length distributions are broadly similar for sizes larger than 1 km, but CALIOP samples more large clouds (Fig. 9). This is because HSRL is able to sample smaller clouds than CALIOP can resolve and such clouds comprise 55% of the clouds sampled by HSRL. Sub-sampling HSRL as CALIOP (i.e., we subsample HSRL profiles every ~335 m) shifts the HSRL cloud length distribution to larger sizes, closely matching the CALIOP data (Fig. 9), suggesting that the size distribution difference at cloud lengths smaller than 1 km is primarily due to sparse sampling by CALIOP rather than FOV size differences (HSRL FOV is 60 m; CALIOP FOV is 90 m). CALIOP and HSRL mean f_{cld} values (0.24 and 0.31, respectively) agree to within 2 standard deviations, but $f_{thin,cld}$ values do not agree, being 0.89 (CALIOP) and 0.61 (HSRL). This effect cannot be due to the relative along-track sparsity of CALIPSO sampling. Differences in HSRL and CALIOP cloud detection algorithms may be partly responsible for the $f_{thin,cld}$ disparity (e.g., the HSRL layer detection method may not be well suited to detecting attenuated surface returns). Another likely cause is the narrow HSRL FOV (8 m across-track compared with 60 m along-track), giving rise to the possibility that HSRL will miss some small clouds that lie on either side of the HSRL FOV, but which lie inside the CALIOP FOV (see schematic in Fig. 9, inset). Since smaller clouds tend to be optically-thin, the clouds missed by HSRL are likely to be optically-thin.

The HSRL size distribution in Fig. 9 shows a roll-off at cloud lengths below about 0.5 km. This may be a hint that there exists a lower limitation to the cloud length of the smallest clouds, i.e., a scale break in the cloud length distribution. We note that this length is consistent with the typical length scale of turbulent eddies in the boundary layer. Without further evidence from observations and models we cannot be sure if the scale break is a real physical feature or reflects sampling a mixture of distributions on different days, but very high-resolution large eddy simulations could be used to examine this. We note that

one high-resolution Landsat satellite study [*Sengupta et al*., 1990] reported a scale break in cumulus cloud length distribution at 1 km, with larger (smaller) β observed for larger (smaller) clouds. The scale break was observed at a larger size (1 km) than in the HSRL data shown here (~500 m). Such a scale break is not a universal feature in trade cumulus [*Zhao and Di Girolamo*, 2007]. Further studies with high-resolution airborne lidar would be helpful to understand any physical limits to the population of the smallest clouds.

Cloud lengths at median f_{cld} for the matched HSRL-CALIOP data indicate that L_{50} is 1.3 km for HSRL and 1.7 km for CALIOP. The L_{50} value from two years of CALIOP data for this region is 1.3 km, close to the matched dataset value. This is also consistent with high resolution airborne imaging radiometer measurements in other trade wind regions such as the Indian Ocean [McFarquhar et al. 2004]. We therefore believe that the conclusions we derive (see Section 6) from the HSRL-CALIOP comparison are somewhat representative of trade cumulus regions throughout the tropics.

3.2.3 Cloud Length Distribution and Optically-thin Cloud Cover Variation

Another approach to examine how optically-thin profiles are distributed among clouds of different sizes is to bin, as a function of cloud length L, the fraction of cloudy profiles that are optically thin ($f^{L}_{thin,cld}$). For this we use the entire CALIOP cloud dataset (1.7 million cloud entities). Surprisingly, the function $f^{L}_{thin,cld}$ is almost region-invariant (Fig. 10). As cloud length increases, the fraction of optically-thin profiles comprising that cloud decreases. Clouds of a given horizontal size possess a similar fraction of optically-thin elements regardless of whether they occur in regions dominated by trade wind cumulus or stratocumulus. Approximately 50% of profiles comprising clouds of size L~15 km, as determined by CALIOP, are optically thin. Clouds smaller than 2 km are almost entirely optically thin, whereas clouds larger than 100 km are less than 20% optically thin. A similar relationship is observed in the HSRL data (not shown), but with the HSRL $f^{L}_{thin,cld}$ curve shifted to smaller cloud lengths for reasons discussed in the preceding section.

The near region-invariant nature of $f^{L}_{thin,cld}$ can be explained if each region essentially experiences low clouds of all types, from small cumulus to relatively large sheets of stratocumulus. Visual inspection of visible imagery suggests that this is a reasonable supposition. Surprisingly, each of these cloud types appears to have very similar characteristics in terms of its optical thickness distribution, regardless of location. Clearly, however, the frequency with which each region experiences clouds of different sizes varies dramatically from region to region. This result leads us to ask whether geographical variations in the fraction of clouds that are optically thin might be largely explained by regional differences in the cloud size distribution.

To test this, we make an estimate of the optically-thin fraction of marine low clouds ($\tilde{f}_{thin,cld}$) using a single $f^{L}_{thin,cld}$ function based on the entire non-polar ocean dataset (Fig. 10) together with the 5°x5° binned two-year cloud length distributions $n(L)$ as,

$$\tilde{f}_{thin,cld} = \frac{1}{\int_{L_{min}}^{L_{max}} L\, n(L) dL} \int_{L_{min}}^{L_{max}} f^{L}_{thin,cld} L\, n(L) dL \qquad (2)$$

where $L_{\text{max/min}}$ is the upper/lower CALIOP size range limit and L is the bin center cloud length. We find that over non-polar oceans and separately over the tropics, the cloud length distribution alone explains three-quarters of the variance in $f_{\text{thin,cld}}$ (R^2 = 0.73 and 0.77, respectively). What this result tells us is that knowledge of how the marine low-cloud length distribution of all clouds varies is sufficient to accurately predict the geographical variation in the optically-thin fraction of clouds across most of the ocean. This is important

because it means that the occurrence of optically-thin clouds is inherently tied to the size distribution of all low clouds. Further, it suggests that the processes controlling optically-thin clouds should not be considered as independent of the processes controlling low clouds in general.

3.3 Cloud Vertical Structure

Knowing the vertical distribution of cloud condensate is important for radiative transfer calculations and for model parameterization of cloud overlap. Vertically-resolved (60 m) optically-thin and optically-thick CTH, optically-thin cloud base height (CBH), and optically-thin cloud-layer depth are presented for each of the three regions/regimes discussed previously (Section 3.2; Table 3). Note that CBH cannot be observed for optically-thick clouds as, by definition, the lidar signal is fully attenuated by the cloud. The dynamical processes associated with each cloud regime are as follows: The vertical development of marine stratocumulus is suppressed by subsidence associated with either the descending branch of the Hadley/Walker circulation or subsiding air masses associated with mid-latitude cyclones, depending upon location. As a result, the marine stratocumulus layer is capped by a strong temperature inversion, resulting in extensive low clouds [*Klein and Hartmann,* 1993]. As the stratocumulus air mass moves equatorward it is advected over warmer sea-surface temperatures (SSTs), surface latent heat fluxes increase, and the subsequent transition to a cumulus regime is explained by the deepening-warming mechanism proposed by *Wyant and Bretherton* [1997]. Consistent with a deepening marine boundary layer from stratocumulus to trade cumulus, both optically-thin and optically-thick CTH distributions peak at higher altitudes transitioning from a stratiform to a convective type cloud regime (Fig. 11a-11c).

In the stratocumulus region, optically-thick CTH peaks at twice the altitude observed for optically-thin clouds (1.2 km and 0.6 km, respectively). Although cloud cover in stratocumulus regions is dominated by optically-thick cloudy profiles (Fig. 5c), optically-thin cloudy profiles comprise greater than 95% of clouds up to 4 km in size (Fig. 10). Together, this suggests that small clouds typically have lower CTH than larger, optically-thicker clouds. Noting that estimates of stratocumulus depth range from 200-300 m in the subtropics and tropics [*Wood*, 2011], and that optically-thin cloud-layers preferentially reside in the lowest 1 km with mean depth of 200 m (Fig. 12a), we suggest that incidences of optically-thin CTH below 1 km in this stratocumulus region are separate cloud entities from the optically-thicker clouds with CTH greater than 1 km. Many of these likely reflect expansive collapsed boundary layers and fog layers (note occurrence of very low-cloud bases in Fig. 11d and data along the 1:1 line in Fig. 12a) that occur periodically in regions dominated by marine stratocumulus [*Ackerman et al.*, 1993; *Christensen and Stephens*, 2011].

As would be expected given the weakening of the capping inversion and deepening of the marine layer in the transition from stratocumulus to cumulus, optically-thin and optically-thick CTH distributions are shifted upwards relative to the stratocumulus regime (cf. Figs. 11a and 11b). Cloud cover remains largely optically-thick, but in contrast to the stratocumulus region the tops of these layers tend to occur at altitudes closer to the optically-thick layers, suggesting that the optically-thin clouds in the transition region may be largely associated with thinning stratocumulus and stratus layers and remnants of dissipating stratocumuli near the top of the boundary layer.

In the trade wind cumulus region (Fig. 11c and 11f), the modal heights for optically-thin and optically-thick cloudy profiles are again at different levels (0.8 and 2 km respectively). Optically-thin profiles dominate the cloud cover in this regime ($f_{thin,cld}$=0.84),

and clouds are not horizontally extensive (L_{50}=0.96 km). Despite having modes at distinct levels, optically-thin and optically-thick CTH are observed above 400 m up to a height of 3 km (Fig. 11c). Peak optically-thin CBH is ~600 m (Fig. 11f). Detrained elements from optically-thick clouds may account for a large proportion of optically-thin clouds at altitudes greater than 1 km, but the mode in optically-thin clouds below 1 km probably consists of small cumuli and associated fragments of clouds with insufficient buoyancy to grow in stature. An aerial photograph of a trade wind cloud field (Fig. 13) highlights the wide range of horizontal and vertical cloud dimensions found in trade wind regions. Notable is the prevalence of tenuous, wispy clouds with limited vertical extent, along with optically thicker clouds, although the latter are less numerous. The bimodal nature of the combined optically-thin and optically-thick cumulus CTH distributions (sum of both distributions, not shown) agrees well with high-resolution (90 m) satellite observations of trade wind cumulus CTH [*Genkova et al.,* 2007] and with a large-eddy simulation (LES) cloud cover distribution for a non-precipitating trade cumulus case [*Siebesma et al.,* 2003]. This encouragingly suggests that LES is a useful tool to examine macrophysical properties of optically-thin clouds that are the dominant cloud type in the trade wind cloud regimes.

The optically-thin cloud-layer thickness distributions (Fig. 12 insets) are similar for all three regions. The drop-off in frequency of occurrence of layers less than 180 m may be an artifact of the increase in the nighttime optical depth detection threshold for shallow layers, i.e. the threshold is 0.03 for layers greater than 180 m, and 0.1 for shallower layers (Section 2.1). We note, however, that optically-thin cloud layer depth may be overestimated by CALIOP VFM: if a cloud partially fills a 60 m height bin yet has an optical depth greater than 0.1, the entire 60 m bin will be classified as cloudy. This high bias will affect shallow layers more than deep layers, in a relative sense. For example, a 60 m optically-thin cloud partially filling two vertically adjacent 60 m bins, will register as 120 m in depth, an error of 100%, whereas, an optically-thin cloud-layer occupying four 60 m bins, and partially-filling a fifth bin by 50% will have a layer depth relative error of ~11%. Conservatively assuming the maximum error of 60 m in layer depth yields a 25% potential overestimate of mean optically-thin cloud-layer depth. Irregular or inhomogeneous clouds e.g., trade cumulus, will be most prone to this error. A recent LES study investigating the effects of cumulus cloud irregularity on cloud overlap quantified the effect of partially filled model levels as a function of model vertical resolution [*Neggers et al*., 2011]. Employing their formulation at CALIOP VFM cloud-layer boundary detection resolution (60 m) produces a high-bias estimate of 28%, which is very similar to our own estimate.

4.0 Discussion

Our findings point to a prevalence of optically-thin low clouds over the oceans, even at the scale of individual CALIOP lidar profiles. While this might be expected at the scale of typical moderate resolution passive visible remote sensors used to construct cloud climatologies, our prior expectation was that most of the optically-thin cloudy pixels from these moderate-resolution passive sensors would be partially filled by small cumulus covering only a small fraction of the pixel, and that the clouds themselves might have considerably higher optical thicknesses than the pixel as a whole. This appears not to be the case, and it prompts us to ask whether even the CALIOP FOVs are partially filled with yet smaller clouds. Given that there are many single-profile cloud entities in the CALIOP dataset (Figs. 7 and 9), it is possible a significant fraction of these profiles are partially filled.

The cloud within any CALIOP partially filled field of view (pFOV) could be optically-thick or optically-thin. Based upon CALIOP data alone, we cannot diagnose whether or not a cloudy FOV is partially cloud-filled, nor can we determine if the cloud-filled part is optically-thick or optically-thin. Classifying a pFOV as optically-thin when the cloud intercepted is optically-thick cloud will lead to an overestimate of $f_{\text{thin,cld}}$. To investigate the frequency of pFOVs, and whether or not the clouds partially filling the lidar FOVs are optically-thick, we employ a simple bounded cascade fractal model.

4.1 Bounded Cascade Model Description

The theoretical basis for, and an in-depth description of the model is presented by *Marshak et al.* [1994] and its application to simulating one-dimensional cloud fields is provided by *Wood and Field* [2011]. A brief description follows. A one-dimensional multiplicative cascade broken cloud field is generated by initially assuming a uniform value of a cloud property; here, optical depth. The field is bisected, and each half is scaled by a factor $1\pm w_i$, with the gaining half chosen at random. This is repeated for each half, and so on, with weighting factors (w_i) calculated for each step i as,

$$w_i = \frac{(1-2p)}{2^{H(i-1)}} \quad (3)$$

where p ($0 < p < 0.5$) controls the intermittency of the resulting optical depth field, and H ($0 < H < \infty$) is a scaling factor representing the smoothness of the field. This simple model has displayed skill in representing scaling properties of marine stratocumulus liquid water content [*Marshak et al.,* 1997; *Davies et al.,* 1999], and regional-global cloud size statistics derived from the cloud optical depth field [*Wood and Field,* 2011]. Specifically, it is shown in the latter case that the power law exponent β in the cloud chord length distribution is inversely related to the value of H controlling the optical depth field, such that smooth fields (large H) are associated with more large clouds and low β, and vice versa.

The model is used to generate 100 optical depth realizations, each with 17 cascade steps and therefore 2^{18} individual data points of horizontal scale 2.8 m and total length 700 km. This large range of scales is chosen so that we can (a) use the model to explore sub-FOV variability within the CALIOP FOV (we have 32 model pixels in the 90 m FOV); (b) have sufficiently long transects to provide good statistics and be approximately consistent with the aggregation scale for our CALIOP analysis. Consecutive FOVs are separated by 335 m to be consistent with CALIOP sampling. We correct all modeled cloud length distributions for sampling bias associated with clouds approaching the limited transect length using Eq. (1).

The optical depth threshold for CALIOP cloud detection ($\tau_{\text{cld,thresh}}$=0.03) is applied to determine if a given model FOV is cloudy. If a surface is detected by CALIOP in the presence of a cloud, it is not known *a priori* whether the cloud is optically thin, or if an optically-thick cloud is partially filling the FOV. To determine if CALIOP would detect the surface for any given cloudy model FOV (i.e., to determine if the FOV would be classified as optically thin cloud), we compare the number of surface-returned photons (n) that would be obtained from a model-simulated cloudy FOV to the *minimum* number of surface-returned photons (n_*) required to detect the surface. If the surface returns N photons without cloud attenuation, then from Beer's law, $n = Ne^{-2\tau}$. This ignores multiple scattering, which is weak for optically-thin clouds. We know that the surface is *just* detected in the presence of a uniform cloud with τ_*=3, and so $n_* = Ne^{-2\tau_*}$, which gives $n/n_* = e^{-2(\tau_* - \tau)}$. We compute n/n_* for every model pixel (2.8 m scale) and then take the mean over the CALIOP FOV. If this FOV mean $\overline{n/n_*}$ >1 then the surface would be detected and

such a cloudy FOV is classified as optically thin to best match our CALIOP observational definition.

We focus our investigation on our representative tropical Pacific trade wind region (Table 3) because the trades have the smallest marine low clouds (Fig. 8a) and are therefore the most prone to the partially filled FOV problem [*Jones et al.,* 2012]. Experimentation shows that model settings best simulating CALIOP observations are $p = 0.0005$, $H = 0.07$, with scene mean optical depth (also a specified input variable) set to 4.5, selected as follows. Because H is closely related to β (Fig. 15; *Wood and Field*, [2011]), we vary H to match CALIOP observed β (Fig. 14). We also vary p to match observed CALIOP trade wind region mean f_{cld} and $f_{thin,cld}$ as closely as possible. Finally, scene mean optical depth is adjusted such that TOA albedo α_{TOA} estimated from model τ_{cld} values, falls within the range of CERES albedo values for this region. Calculation details are presented in full in Table 4.

4.1.1 Model Simulation of Observed Cloud Properties

The model demonstrates skill in generating realistic representations of CALIOP observed cloud properties f_{cld} and $f_{thin,cld}$, β and TOA albedo α^{TOA} (Table 4). Consistency between observed (CALIOP) and predicted cloud size distributions suggests that optically-thin cloud behavior is broadly consistent with a power law scaling of optical depth: this scaling is an underlying assumption of the model. For comparison, we also sample the model output simulating MODIS and HSRL FOV (1 km and 60 m along-track dimensions, respectively). HSRL-simulated model output is uses the same $\tau_{cld,thresh}$=0.03 and $n/n_* > 1$ thresholds used for CALIOP. We set MODIS $\tau_{cld,thresh}$ to be 0.4 [*Ackerman et al.,* 2008], with $\tau_{thin,thresh}$ as for CALIOP. Perhaps unexpectedly, model simulated MODIS f_{cld} is 1.5 times *lower* than CALIOP and HSRL simulated f_{cld} (Table 4). Varying MODIS $\tau_{cld,thresh}$ within reasonable limits (0.2 to 0.6) produces model simulated MODIS f_{cld} values of 0.20 and 0.14 respectively (i.e. still lower than the CALIOP value of 0.27). We therefore suggest that overestimation of cloud cover using passive visible imagers (e.g.*, Zhao and Di Girolamo,* [2006]) may not necessarily always occur. Rather, the bias depends sensitively upon cloud length and the reflectance threshold applied.

As instrument resolution increases (FOV size decreases), each simulated size distribution is shifted to smaller sizes (Fig. 14). We note that the model-simulated HSRL cloud length distribution, since it is derived from a bounded cascade, does not reproduce the observed gradual roll-off to a flatter size distribution at cloud lengths smaller than ~500 m seen in the tropical western Atlantic trade wind region (Fig. 9). Interestingly, simulated cloud length distributions for all instrument FOVs have similar β, a result also noted by *Wood and Field* [2011], whereby the cloud length distribution is not strongly sensitive to sensor resolution when the domain to FOV ratio approaches 1000 (i.e. when there is a sufficient range of scales). This ratio is much greater than 1000 for model clouds sampled like CALIOP and HSRL, and is ~1000 in the case of MODIS, and so we would not expect β to be very different across the sensors.

The HSRL has a pulse repetition frequency of 200 Hz, and so prior to averaging, the data have less than 1 m along-track sampling resolution for an aircraft flight speed of 120 m s^{-1}. Although onboard averaging means that we do not actually have observations at this resolution from HSRL, it is interesting to see whether size distributions using higher resolution cloud masks would be shifted to even smaller sizes. The model results suggest that observations at CALIOP and HSRL resolution both miss finer scale cloud length variations, and overestimate cloud lengths (Fig. 14). Additionally, even cloud cover estimates made at CALIOP and HSRL resolution may overestimate f_{cld} by almost 25% in

trade wind regions (Table 4). Although these model results require verification, especially the model behavior at small scales, we note that a four-fold overestimate in f_{cld} was estimated from high-resolution (15 m) trade Cu observations when sensor resolution was degraded to 1 km while cloud detection threshold was held constant [*Dey et. al.,* 2008]. Indeed, this suggests that the very concept of cloud cover may be so sensitive to sensor resolution and detection sensitivity in the trades that it serves no useful function in these regions. For lower resolution sensors (e.g., MODIS) such small-scale clouds likely produce cloud-contamination in clear FOVs [*Koren et al.,* 2007], biasing clear-sky retrievals.

4.2 Partially Filled Fields of View

As previously mentioned, a CALIOP FOV may be misidentified as optically-thin if partially filled by an optically-thick cloud. The model is employed to identify simulated CALIOP cloudy FOVs that are partially cloud filled (pFOV), i.e., not all 32 optical depth values comprising the FOV exceed the threshold for cloud detection ($\tau_{cld,thresh}$). As discussed in Section 4.1, if the FOV-mean ratio of surface-backscattered photons detected by the sensor (n) to the minimum number required for surface detection (n_*) is greater than one, the cloudy FOV is classified as optically thin. The mean n/n_* for the entire pFOV is calculated, along with the mean optical depth of the cloud-only segment. For a given pFOV with $n/n_* > 1$ and mean optical depth of the cloud-only segment greater than 3, the pFOV is therefore misclassified as an optically-thin cloud whereas it is really a partially-filled FOV containing an optically thick cloud. The frequency of such misclassification is estimated. Results are binned by cloud length, and presented in Fig. 15.

The fraction of FOVs that are partially cloud filled is high, especially for smaller clouds where it exceeds 0.8. This fraction decreases to around 0.3 for larger clouds (Fig. 15, circles). CALIOP-observed cloud entities consisting of a single profile are therefore almost all likely to be broken clouds. The bin median pFOV cloud fraction, i.e., fraction of a pFOV that is cloud, increases with cloud length, ranging from 0.50 to 0.85 (Fig. 15, squares), consistent with fewer cloud edges being observed as cloud length increases. Despite the prevalence of partially-filled FOVs, the FOVs classified as optically thin typically do contain mainly optically-thin cloud (Fig. 15, diamonds). Summing the fraction of pFOV that are misclassified for each size bin, and weighting this value by the fraction of optically-thin FOVs that are partially filled, it can be concluded that the potential overestimate of $f_{thin,cld}$ is at most 6% for this cloud regime. In addition, the effect of sensor resolution on f_{cld} can be quantified from the model output. The overestimate in f_{cld} caused by assuming that partially cloud-filled FOVs are 100% cloud filled is estimated at ~0.06 in absolute terms. This value is similar to the ratio of model generated CALIOP and HSRL Full Res f_{cld} (0.27/0.22 = 1.23), with the latter representing "true" f_{cld}.

Based upon the model output, which is designed to simulate typical trade wind cumulus conditions, it is concluded that the majority of cloudy CALIOP profiles are indeed partially cloud filled. Rapid fluctuations of cloud particle concentration on scales ~10 m have been measured in situ [*Pawlowska et al.,* 1997], suggesting that this conclusion is physically realistic. These results have implications for the minimum sensor resolution required for cloud observations in regions of broken cloud, as simulated by the model. A recent study suggests that a resolution higher than 45 m is required to accurately determine the cloud cover to within 0.01 for trade cumulus regimes [*Jones et. al.,* 2012]. Our study suggests that the CALIOP FOV size of 90 m leads to an overestimate of some 0.06 in cloud cover in regions of trade cumulus. This is consistent with *Jones et al*. [2012], whose results

(their Fig. 1) suggest a median overestimation of 0.05 for a sensor with a resolution of ~100 m.

4.3 Additional Applications of Cascade Model Output

4.3.1 Are Optically-thin Clouds Adiabatic?

We analyze the model output to investigate the extent to which optically-thin clouds might be considered adiabatic, i.e., liquid water path (*LWP)* values determined by temperature, pressure and cloud thickness alone. Liquid water path for an adiabatic cloud is proportional to cloud-layer depth (h) squared, the adiabatic rate of increase of liquid water with respect to height (assumed to be 2×10^{-3} g m^{-3} km^{-1}) [*Albrecht et al.*, 1990], and the adiabatic fraction (f_{ad}), is defined as the ratio of observed *LWP* to adiabatic *LWP,* which here we assume to be 1. Using model simulated optically-thin cloud optical depth for a trade wind region as before, and assuming a cloud droplet effective radius (r_e) of 10 μm, we estimate $LWP = 2/3\tau\rho_L r_e$ [*Stephens*, 1994], where ρ_L is liquid water density, and derive corresponding adiabatic cloud-layer depth, h. The simulated adiabatic layer depth distribution (not shown) indicates that depths are on the order of a few 10s of meters, with 90% of the values being less than 90 m, much thinner than observed. In addition, if this *LWP* is evenly distributed over a 60 m layer, we estimate that $f_{ad} \sim 0.05$, and ranges from 0.02 to 0.09 when r_e is halved and doubled, respectively. Alternatively, if τ_{cld} is 0.1, layer depth corresponding to an adiabatic *LWP* is 25 m. Therefore, we conclude that the optically-thin cloud-layers are not adiabatic, but are more likely to be diluted cloud fragments, and their *LWP* should not be estimated adiabatically. This is consistent with effects of entrainment on marine layer clouds (e.g., *McFarlane and Grabowski* [2007]). Stochastically-controlled entrainment events essentially dictate the properties of shallow trade cumulus clouds [*Romps and Kuang*, 2010].

4.3.2 Optically-thin Cloud Contribution to TOA Cloud Albedo

We have shown that optically-thin clouds comprise almost one-half of all marine low clouds over non-polar oceans. To investigate the magnitude of their contribution to low-cloud α^{TOA} in trade wind regions at CALIOP FOV resolution, model simulated optical depth is converted to albedo using a simple approximation, $\alpha^{cld} = \tau_{cld} / (\tau_{cld} + 7.7)$ [*Lacis and Hansen*, 1974]), and α^{TOA} is estimated for optically-thin clouds and all low clouds (Table 4). The ratio of these values is expressed per unit of low-cloud cover and per unit of optically-thin cloud cover, and the calculation is repeated at model full-resolution to investigate how optically-thick clouds classified as optically-thin clouds in pFOVs, affect the results.

In addition to the marine cumulus region described in Table 3, two other trade cumulus regions (of equal size) were examined; one in the tropical western Pacific and one in the tropical western Atlantic. For trade wind regions it can be concluded that with observed $f_{thin,cld} > 0.90$, and $f_{cld} \sim 0.20 - 0.30$, optically-thin low clouds can contribute 55-60% to the total low-cloud albedo. However, the range of values obtained from the full-resolution model simulation indicates that the true contribution of optically-thin clouds to low-cloud albedo is more than a factor of two smaller at 23% - 26%.

5.0 Summary and Concluding Remarks

Analysis of two years of CALIOP nighttime data indicates that 45% of marine low clouds with tops below 3 km, over the non-polar oceans, are classified as optically thin such that they do not fully attenuate the CALIOP lidar signal. Few observational data, other than this work, are available on the physical nature of these clouds. Key results from our analysis are as follows:

1) Over the non-polar oceans, optically-thin clouds comprise 0.25 – 0.75 of marine low clouds with cloud top height below 3 km, with a mean of 0.45;
2) The optically-thin fraction of marine low cloud varies inversely with marine low-cloud cover, and reaches a maximum (> 0.80) in trade wind regions;
3) Although the optically-thin fraction of low clouds peaks in trade wind regions, the absolute frequency of occurrence does not strongly vary over the non-polar oceans;
4) In trade wind regions, according to our analysis of CALIOP observations, clouds smaller than 2 km contribute over 50% of the cloud cover;
5) Optically-thin marine low clouds are predominantly small clouds. The cloud length distribution of all clouds explains three-quarters of the geographical variance in the optically-thin fraction of marine low clouds;
6) Over the non-polar oceans, optically-thin low clouds have a mean cloud top height of 1.2 km and a mean thickness of 0.25 km. However, optically-thin cloud-layer depth may be overestimated by 25% due to cloud partially filling the 60 m vertical resolution CALIOP bins;
7) Collocated HSRL and CALIOP data for the tropical western Atlantic trade wind region reveal that many clouds are smaller than can be resolved at CALIOP resolution. This suggests that clouds, especially optically-thin low clouds, may exist globally on finer scales than reported herein;
8) A simple bounded cascade fractal model is used to represent a one-dimensional optical depth distribution for conditions representative of the trade wind regions. Analysis of model output, in conjunction with observations, suggests that:
    a) Optically-thin low-cloud properties are consistent with a power law scaling of optical depth;
    b) CALIOP fields of view partially filled with optically-thick low cloud produce a potential 6% overestimate in optically-thin fraction of marine low-cloud values in trade cumulus regions;
    c) Optically-thin cloud layer thicknesses are not adiabatic with greater than 90% of simulated optically-thin adiabatic cloud depths less than 90 m, whereas observations indicate much greater thicknesses;
    d) In trade cumulus regions, we estimate that optically-thin low clouds contribute almost a quarter of the albedo contributed by low clouds, but a more sophisticated quantification using radiative transfer modeling is required to confirm this.

Remote sensing of clouds provides global information on cloud macrophysical and microphysical properties, both of which are important for radiative transfer calculations and verification of model representation of clouds. Differences in cloud properties retrieved by ISCCP and MODIS [*Pincus et al.,* 2010] and ISCCP, MODIS and MISR [*Marchand et al.,* 2010] highlight the difficulties inherent in passive remote sensing of low clouds. *Pincus et al.* [2012] reported that ISSCP and MODIS views of clouds are consistent for all but the

optically-thinnest clouds, while sub-pixel scale and broken low-level clouds were identified by *Marchand et al.* [2010] as one of the reasons for discrepancies in cloud properties.

It is known that low clouds are the dominant contributor to the global albedo [*Hartmann et al.,* 1992]. Results from our work indicate that almost half of low clouds over the non-polar ocean are optically thin. Additionally, in trade wind regions, 50% of the low-cloud cover is comprised of clouds less than 2 km in length. Because such a large fraction of cloud is optically thin, even with CALIOP's 90 m footprint size, it is doubtful that the passive sensors are actually determining the coverage of the optically-thick or optically-thin clouds correctly. It is difficult therefore, to conclude that we yet have a precise understanding of the shape of the true cloud optical depth probability distribution function on a global scale, and especially in trade wind regions.

Although CALIOP data do not provide vertically-resolved high resolution off-track spatial context for the cloud fields sampled, such data in the along-track direction afford new insights on the nature of optically-thin clouds. Suggestions for design of future combined active and passive remote sensors would include an array of lasers providing a swath of vertically-resolved data with, ideally, horizontal resolution of a few tens of meters or less, in the across-track and along-track directions, and collocated visible imagery with the same horizontal resolution. Such a configuration would provide collocated profiles of cloud properties, and high-resolution TOA reflectance data to better observe these optically-thin clouds, that comprise almost half of all marine low clouds.

Acknowledgements

This work was supported by NASA award numbers NNX10AE59G and NNX10AN78G. We wish to thank Sarah Doherty for insightful comments which contributed greatly to the quality of this work, and Roger Marchand for pointing out an important flaw in our original application of the bounded cascade model.

References

Ackerman, A.S., O.B. Toon, and P.V. Hobbs (1993) Dissipation of marine stratiform clouds and collapse of the marine boundary layer due to the depletion of cloud condensation nuclei by clouds, *Science*, *262*, 226-229, doi:10.1126/science.262.5131.226.

Ackerman, S., R. E. Holz, R. Frey, E. W. Eloranta, B. C. Maddux, and M. McGill (2008), Cloud Detection with MODIS. Part II: Validation, *J. Atmos. Oceanic Technol.*, *25*, 1073-1086.

Albrecht, B. A., C. W. Fairall, D. W. Thomson, A. B. White, J. B. Snider, and W. H. Schubert (1990), Surface-based remote sensing of the observed and the Adiabatic liquid water content of stratocumulus clouds, *Geophys. Res. Lett.*, *17*, 89–92, doi:10.1029/GL017i001p00089.

Albrecht, B. A., M. P. Jensen, and W. J. Syrett (1995), Marine boundary layer structure and fractional cloudiness, *J. Geophys. Res., 100*, D7, 14,209-14,222.

Bender, F. A-M., R. J. Charlson, A. M-L. Ekman, and L. V. Leahy (2011), Quantification of monthly mean, regional scale albedo of marine stratiform clouds in satellite observations and GCMs, *J. Appl. Meteor. Clim.*, doi: 10.1175/JAMC-D-11-049.1

Benner, T. C., and J. A. Curry (1998), Characteristics of small tropical cumulus clouds and their impact on the environment, *J. Geophys. Res., 103*, D22, 25,752-28,767.

Bucholtz, A. (1995), Rayleigh-scattering calculations for the terrestrial atmosphere, *Appl. Opt.*, *34*, 2,765-2,773.

Charlson, R. J., A. S. Ackerman, F. A-M. Bender, T. L. Anderson, and Z. Liu (2007), On the climate forcing consequences of the albedo continuum between cloudy and clear air, *Tellus*, *59*, 715-727, doi:10.1111/j.1600-0889.200700297.x.

Davies, A. B., A. Marshak, H. Gerber, and W. J. Wiscombe (1999), Horizontal structure of marine boundary layer clouds from centimeter to kilometer scales, *J. Geophys. Res.*, *104*, D6, 6,123-6,144.

Dey, S., L. Di Girolamo, and G. Zhao (2008), Scale effect on statistics of the macrophysical properties of trade wind cumuli over the tropical western Atlantic during RICO, *J. Geophys. Res., 113*, D24214, doi: 10.1029/2008JD010295.

Efron, B., and G. Gong (1983), A Leisurely Look at the Bootstrap, the Jackknife, and Cross-Validation, *The American Statistician*, *37*, 36-48.

Genkova, I., G. Seiz, P. Zuidema, G. Zhao, and L. Di Girolamo (2007), Cloud top height comparisons from ASTER, MISR, and MODIS for trade wind cumuli, *Remote Sens. Environ.*, *107*, 211-222.

Garrett, T. J., and C. F. Zhao (2006), Increased Arctic cloud longwave emissivity associated with pollution from mid-latitudes, *Nature, 440*, 787-789.

Hair, J. W., C. A. Hostetler, A. L. Cook, D. B. Harper, R. A. Ferrare, T. L. Mack, W. Welch, L. R. Izquierdo, and F. E. Hovis (2008), Airborne High Spectral Resolution Lidar for profiling aerosol optical properties, *Appl. Opt.*, *47*, 6,734-6,752.

Harrison, E. F., P. Minnis, B. R. Barkstrom, V. Ramanathan, R. D. Cess, and G. G. Gibson (1990), Seasonal variation of cloud radiative forcing derived from the Earth radiation budget experiment, *J. Geophys. Res*., *95*, 18687–18703.

Hartmann, D. L., M. E. Ockert-Bell, and M. L. Michelsen (1992), The Effect of Cloud Type on Earth's Energy Balance: Global Analysis, *J. Climate*, *5*, 1281–1304, doi: 10.1175/1520-0442(1992)005.

Hozumi, K., T. Harimaya, and C. Magono (1982), The Size Distribution of Cumulus Clouds as a Function of Cloud Amount, *J. Meteor. Soc. Japan, 60*, 691-699.

Hunt, W.H., D. M. Winker, M. A. Vaughan, K. A. Powell, P. L. Lucker, C. Weimer (2009), CALIPSO Lidar Description and Performance Assessment, *J. Atmos. Oceanic Technol.*, *26*, 1214–1228, doi: 10.1175/2009JTECHA1223.1.

Jones, A. L., L. Di Girolamo, and G. Zhao (2012), Reducing the resolution bias in cloud fraction from satellite derived clear-conservative cloud masks, *J. Geophys. Res., 117*, D12201, doi:10.1029/2011JD017195, in press.

Kacenelenbogen. M., M. A. Vaughan, J. Redemann, R. M. Hoff, R. R. Rogers, R. A. Ferrare, P. B. Russell, C. A. Hostetler, J. W. Hair, and B. N. Holben (2011), An accuracy assessment of the CALIOP/CALIPSO version 2/version 3 daytime aerosol extinction product based on a detailed multi-sensor, multi-platform case study, *Atmos. Chem. Phy.*, *11*, 3,981-4,000, doi:10.5194/acp-11-3981-2011.

Kay, J. E., Hillman, B., Klein, S., Zhang, Y., Medeiros, B., Gettelman, G., Pincus, R., Eaton, B., Boyle, J., Marchand, R. and T. Ackerman (2012), Exposing global cloud biases in the Community Atmosphere Model (CAM) using satellite observations and their corresponding instrument simulators, *J. Climate*, doi:10.1175/JCLI-D-11-00469.1, in press.

Klein, S. A., and D. L. Hartmann (1993), The Seasonal Cycle of Low Stratiform Clouds, *J. Climate.*, *6*, 1,587-1,606.

Koren, I., L. A. Remer, Y. J. Kaufman, and Y. Rudich (2007), On the twilight zone between clouds and aerosols, *Geophys. Res. Lett.*, *34*, L08805, doi:10.1029/2007GL029253.

Koren, I., L. Oreopoulos, G. Feingold, L. A. Remer, and O. Attaratz (2008), How small is a small cloud?, *Atmos. Chem. Phys.*, *8*, 3,855-3,864.

Koren, I., G. Feingold, H. Jiang, and Orit Altaratz (2009), Aerosol effects on the inter-cloud region of a small cumulus cloud field, *Geophys. Res. Lett.*, *36*, L14805, doi:10.1029/2009GL037424.

Lacis, A. A., and J. E. Hansen (1974), A Parameterization for the Absorption of Solar Radiation in the Earth's Atmosphere, *J. Atmos. Sci.*, *31*, 118-133.

Marshak, A., A. Davis, R. Cahalan, and W. Wiscombe (1994), Bounded cascade models as nonstationary multifractals, *Phys. Rev. E*, *49(1)*, 55-69.

Marshak, A., A. Davis, W. Wiscombe, and R. Cahalan (1997), Scale invariance in liquid water distributions in marine stratocumulus. Part II: multifractal properties and intermittency issues, *J. Atmos. Sci.*, *54*, 1,423-1,444.

Masonis, S. J., T. L. Anderson, and D. S. Covert (2003), A Study of the Extinction-to-Backscatter Ratio of Marine Aerosol during the Shoreline Environment Aerosol Study, *J. Atmos. Oceanic Technol.*, *20*, 1,388-1,402.

McFarlane, S. A., and W. W. Grabowski (2007), Optical properties of shallow tropical cumuli derived from ARM ground-based remote sensing, *Geophys. Res. Lett., 34*, L06808, doi:10.1029/2006GL028767.

McFarquhar, G. M., S. Platnick, L. Di Girolamo, H. Wang, G. Wind, and G. Zhao (2004), Trade wind cumuli statistics in clean and polluted air over the Indian Ocean from in situ and remote sensing measurements, Geophys. Res. Lett., 31, L21105, doi:10.1029/2004GL020412.

Medeiros, B., L. Nuijens, C. Antoniazzo, and B. Stevens (2010), Low-latitude boundary layer clouds as seen by CALIPSO, *J. Geophys. Res., 115*, D23207, doi:10.1029/2010JD014437.

Neggers, R. A. J., T. Heus, and A. P. Siebesma (2011), Overlap statistics of cumuliform boundary-layer cloud fields in large-eddy simulations, *J. Geophys. Res., 116*, D21202, doi:10.1029/2011JD015650.

965 Pawlowska, H., J. L. Brenguier, and G. Salut (1997), Optimal Nonlinear Estimation for
966 Cloud Particle measurements, *J. Atmos. Oceanic Technol.*, *14*, 88-104.
967 Pincus, R. S., S. Platnick, S. Ackerman, R. Hemler, and R. Hofmann (2012), Reconciling
968 simulated and observed views of clouds: MODIS, ISCCP, and the limits of instrument
969 simluators, *J. Climate,* doi:10.1175/JCLI-D-11-00267.1, in press.
970 Plank, V. G. (1969), The size distribution of cumulus clouds in representative Florida
971 populations, *J. Appl. Meteorol*., 8, 46– 67.
972 Redemann, J., Q. Zhang, P. B. Russell, and J. M. Livingston (2009), Case studies of aerosol
973 remote sensing in the vicinity of clouds, *J. Geophys. Res.*, *114*, D06209,
974 doi:10.1029/2008JD010774.
975 Rogers, R. R., C. A. Hostetler, J. W. Hair, R. A. Ferrare, Z. Liu, M. D. Obland, D. B.
976 Harper, A. L. Cook, K. A. Powell, M. A. Vaughan, and D. M. Winker (2011),
977 Assessment of the CALIPSO Lidar 532 nm attenuated backscatter calibration using the
978 NASA LaRC airborne High Spectral Resolution Lidar, *Atmos. Chem. Phys.*, *11*, 1,295-
979 1,311, doi:10.5194/acp-11-1295-2011.
980 Romps, D. M., and Z. Kuang (2010), Nature versus nurture in shallow convection, *J. Atmos.*
981 *Sci.*, *67*, 1655-1666.
982 Rossow, W. B., and R. A. Schiffer (1999), Advances in Understanding Clouds From
983 ISCCP, *Bull. Am. Meteorol. Soc.*, *80(11)*, 2,261-2,287.
984 Rossow, W.B., C. Delo, and B. Cairns (2002), Implications of the observed mesoscale
985 variations of clouds for the Earth's radiation budget, *J. Climate*, *15*, 557-585.
986 Sengupta, S. K., R. M. Welch, M. S. Navar, T. A. Berendes, and D. W. Chen (1990),
987 Cumulus Cloud Field Morphology and Spatial Patterns Derived from High Spatial
988 Resolution Landsat Imagery, *J. App. Meteor.*, *29*, 1,245-1,267.
989 Siebesma, A. P., C. S. Bretherton, A. Brown, A. Chlond, J. Cuxart, P. G. Duynkerke, H.
990 Jiang, M. Khairoutdinov, D. L., Lewellen, C-H. Moeng, E. Sanchez, B. Stevens, and D.
991 E. Stevens (2003), A Large Eddy Simulation Intercomparison Study of Shallow
992 Cumulus Convection, *J. Atmos. Sci.*, *60(10)*, 1,201-1,219.
993 Smirnov, A., B. N. Holben, Y. J. Kaufman, O. Dubovik, T. F. Eck, I. Slutsker, C. Pietras,
994 and R. N. Halthore (2002), Optical Properties of Atmospheric Aerosol in Maritime
995 Environments, *J. Atmos. Sci.*, *59*, 501-523.
996 Stephens. G. L. (1994), Remote Sensing of the Lower Atmosphere. Oxford University
997 Press, 523 pp.
998 Su, W., G. L. Schuster, N. G. Loeb, R. R. Rogers, R. A. Ferrare, C. A. Hostetler, J. W. Hair,
999 and Michael D. Obland (2008), Aerosol and cloud interactions observed from high
1000 spectral resolution lidar data, *J. Geophys. Res.*, *113*, D24202,
1001 doi:10.1029/2008JD010588.
1002 Tackett, J. L, and L. Di Girolamo (2009), Enhanced aerosol backscatter adjacent to tropical
1003 trade wind clouds revealed by satellite-based lidar, *Geophys. Res. Lett.*, *36*, L14804,
1004 doi:10.1029/2009GL039264.
1005 Turner, D. D, A. M. Vogelmann, R. T. Austin, J. C. Barnard, K. Dacy-Pereira, J. C. Chiu, S.
1006 A. Clough, C. Flynn, M. M. Kahiyer, J. Liljegren, K. Johnson, B. Lin, C. Long, A.
1007 Marshak, S. Y. Matrosov, S. A. McFarlane, M. Miller, Q. Min, P. Minnis, W. O'Hirok,
1008 Z. Want, and W. Wiscombe (2007), Thin Liquid Water Clouds – Their importance and
1009 our challenge, *Bull. Am. Meteorol. Soc.*, *88(2)*, 177-190, doi:10.1175/BAMS-88-2-177.
1010 Twohy, C. H., J. A. Coakley Jr., and W. R. Tahnk (2009), Effect of changes in relative
1011 humidity on aerosol scattering near clouds, *J. Geophys. Res.*, *114*, D05205,
1012 doi:1029/2008JD010991.

1013 Várnai, T, and A. Marshak (2009), MODIS observations of enhanced clear sky reflectance
1014 near clouds, *Geophys. Res. Lett., 36*, L06807, doi:10.1029/2008GL037089.
1015 Várnai, T, and A. Marshak (2011), Global CALIPSO Observations of Aerosol Changes
1016 Near Clouds, *IEEE Geosci. Remote Sens. Lett.*, *8(1)*, 19-23.
1017 Vaughan, M. A., D. M. Winker, and K. A. Powell (2005), Part 2:Feature Detection and
1018 Layer Properties Algorithms. CALIOP Algorithm Theoretical Basis Document PC-
1019 SCI-202.01, 87 pp. [Available online at http://www-
1020 calipso.larc.nasa.gov/resources/pdfs/PC-SCI-202_Part2_rev1x01.pdf].
1021 Vaughan, M. A., K. A. Powell, R. E. Kuehn, S. A. Young, D. M. Winker, C. A. Hostetler,
1022 W. H. Hunt, Z. Liu, M. J. McGill, and B. J. Getzewich (2009), Fully Automated
1023 Detection of Cloud and Aerosol Layers in the CALIPSO Lidar Measurements, *J. Atmos.*
1024 *Oceanic Technol.*, *26*, 2,034-2,050, doi: 10.1175/2009JTECHA1228.1.
1025 Wen, G., A. Marshak, R. E. Cahalan, L. A. Remer, and R. G. Gleidman (2007), 3-D
1026 aerosol-cloud radiative interaction observed in collocated MODIS and ASTER images
1027 of cumulus cloud fields, *J. Geophys. Res.*, *112*, D13204, doi:10.1029/2006JD008267.
1028 Wielicki, B. A., and R. M. Welch (1986), Cumulus Cloud Properties Derived Using Landsat
1029 Satellite Data, *J. Clim. Appl, Meteorol.*, *25*, 261-276.
1030 Winker, D. M., M. A. Vaughan, A. Omar, Y. Hu, K. A. Powell, Z. Liu, W. H. Hunt, and S.
1031 A. Young (2009), Overview of the CALIPSO Mission and CALIOP Data Processing
1032 Algorithms, *J. Atmos. Oceanic Technol.*, *26*, 2310–2323, doi:
1033 10.1175/2009JTECHA1281.1.
1034 Winker, D. M., J. Pelon, J. A. Coakley, S. A. Ackerman, R. J. Charlson, P. R. Colarco, P.
1035 Flamant, Q. Fu, R. M. THE CALIPSO MISSION A Global 3D View of Aerosols and
1036 Clouds, *Bull.Am. Meteorol. Soc.*, *91*, 1,211-1,229, doi:10.1175/2010BAMS3009.1.
1037 Wood. R., and J. P. Taylor (2001), Liquid water path variability in unbroken marine
1038 stratocumulus cloud, *Quart. J. Roy. Meteor. Soc., 127*, 2,635-2,662.
1039 Wood, R., and C. S. Bretherton (2004), Boundary layer Depth, Entrainment, and
1040 Decoupling in the Cloud-Capped Subtropical and Tropical marine Boundary Layer, *J.*
1041 *Climate*, *17*, 3,576-3,588.
1042 Wood, R., and D. L. Hartmann (2006), Spatial Variability of Liquid Water Path in Marine
1043 Low Cloud: The Importance of Mesoscale Cellular Convection, *J. Climate, 19*, 1,748-
1044 1,764.Wood, R., and P. R. Field (2011), The Distribution of Cloud Horizontal Sizes, *J.*
1045 *Climate.*, *24*, 4,800–4,816, doi: 10.1175/2011JCLI4056.1.
1046 Wood, R. (2011) Stratocumulus Clouds, *Mon. Wea. Rev.,* doi:10.1175/MWR-D-11-
1047 00121.1, in press.
1048 Wyant, M. C., C. S. Bretherton, H. A. Rand, and D. E. Stevens (1997) Numerical
1049 Simulations and a Conceptual Model of the Stratocumulus to Trade Cumulus Transition,
1050 *J. Atmos. Sci.*, *54*, 168–192.
1051 Zhang, J., and J. S. Reid (2005), An analysis of potential cloud artifacts in MODIS over
1052 ocean aerosol optical thickness products, *Geophys. Res. Lett.*, *32*, L15803,
1053 doi:10.1029/2005GL023254.
1054 Zhao, G., and L. Di Girolamo (2006), Cloud fraction errors for trade wind cumuli from
1055 EOS-Terra instruments, *Geophys. Res. Lett.*, *33*, L20802, doi:10.1029/2006GL028088.
1056 Zhao, G., and L. Di Girolamo (2007), Statistics on the macrophysical properties of trade
1057 wind cumuli over the tropical western Atlantic, *J. Geophys. Res.*, *112*, D10204,
1058 doi:10.1029/2006JD007371.

Zuidema, P., D. Leon, A. Pazmany, and M. Cadeddu (2012), Aircraft millimeter-wave passive sensing of cloud liquid water and water vapor during VOCALS-REx, *Atmos. Chem. Phy.*, *12*, 355-369, doi:10.5194/acp-12-355-2012.

TABLES

Table 1. CALIOP – HSRL matched dataset description. [a]

Date	Location[b]	Overpass Time[c]	Cloud Type[d]
26 Jan 2007	36.88°N, 75.52°W	07:11	-
23 May 2007	32.41°N, 77.07°W	18:32	Cumulus
26 Jan 2008	12.43°N, 60.26°W	17:36	Cumulus
11 Aug 2010	33.59N, 65.09W	17:43	Cumulus/Stratocumulus
18 Aug 2010	22.38°N, 63.95°W	17:48	Cumulus
22 Aug 2010	13.71°N, 69.04°W	06:39	-
24 Aug 2010	21.76°N, 64.09°W	06:15	-
26 Aug 2010	20.67N, 61.25W	06:02	-

[a] Transect lengths range from 34 km to 215 km, with an 8-day mean of 126 km.
[b] Segment mid-point (latitude, longitude).
[c] Times are UTC.
[d] Cloud type information from inspection of MODIS Aqua L1B Granule Images (daytime only), (http://modis-atmos.gsfc.nasa.gov/IMAGES/index_myd021km.html).

Table 2. Cloud cover[a] definitions for this work.

Parameter[b]	**Definition**	**Equation**[c]
Low-cloud cover (f_{cld})	The fraction of all high-cloud-screened clear and cloud profiles within a gridbox that are clouds.	$\sum N_{cloud} \Big/ \sum (N_{clear} + N_{cloud})$
Optically-thin low-cloud cover (f_{thin})	The fraction of all high-cloud-screened clear and cloud profiles within a gridbox that are optically-thin.	$\sum N_{thin} \Big/ \sum (N_{clear} + N_{cloud})$
Optically-thin fraction of low cloud ($f_{thin,cld}$) i.e. $f_{thin} / f_{cld} = f_{thin,cld}$	The fraction of high-cloud-screened cloud profiles within a gridbox that are optically-thin.	$\sum N_{thin} \Big/ \sum N_{cloud}$

[a] Unless otherwise stated, all gridbox cloud cover values are two-year averages of monthly calculated values.

[b] All parameters are calculated at full-resolution.

[c] N is the number of full-resolution profiles within a gridbox that are: cloudy (N_{cloud}), cloudy and optically-thin (N_{thin}), clear (N_{clear}).

1078 **Table 3.** Stratocumulus (Sc), Cumulus (Cu), and transition from Sc to Cu regime
1079 (Sc-Cu), region details: location, low-cloud cover (f_{cld}), optically-thin fraction of low
1080 cloud ($f_{\mathrm{cld,thin}}$).

Cloud Type	Latitude	Longitude	f_{cld} [a,b]	$f_{\mathrm{thin,cld}}$ [a,b]
Sc	20°N - 30°N	120°W - 130°W	0.79	0.36
Sc-Cu	10°N - 15°N	130°W - 140°W	0.70	0.37
Cu	10°S - 20°S	150°W - 160°W	0.26	0.84

1081 [a] f_{cld} and $f_{\mathrm{cld,thin}}$ are two-year means of monthly values. N = 96 (24 months x 4 gridbox values)
1082 [b] f_{cld} and $f_{\mathrm{cld,thin}}$ sampling uncertainties are 0.02 – 0.04 (95% confidence level), and are estimated from the
1083 bootstrap method [*Efron and Gong,* 1983].
1084

Table 4. Cumulus cloud-field observed and modeled parameters.

Instrument	f_{cld}	$f_{thin,cld}$	β[a]	α_{TOA}[b]
Observed:				
CALIOP	0.26(0.11)[c]	0.84(0.13)[c]	2.66±0.43	
CERES				0.16
MODIS				0.11
Model[d]				
CALIOP	0.27	0.93	2.42±0.62	0.16
HSRL	0.26	0.93	1.93±0.12	-
HSRL full-res[e]	0.22	0.79	2.13±0.14	-
MODIS	0.16	0.95	1.97±0.19	-

[a] Cloud length distribution power law exponent±95% CI.

[b] Top-of-atmosphere albedo (α^{TOA}) values are used to constrain model mean (clear and cloudy) optical depth. CERES shortwave TOA albedo (*http://eos.atmos.washington.edu/cgi-bin/ceres/disp.pl?ceres.alb.ann.d*) and MODIS reflectance (R_{MODIS}) estimated as $R_{MODIS} = R_{cld} f_{cld} + R_{clr} f_{clr}$, where R_{cld} is mean visible cloud reflectance [*Wood and Field*, 2011] at 1 km cloud length (minimum observable MODIS cloud length), R_{clr} is a typical visible clear-sky reflectance (0.08), and f_{cld},and f_{clr} weights are CALIOP observed cloud and clear fractions, for the tropical Pacific trade wind cumulus region [15°S, 155°W; center latitude, longitude]. We estimate model TOA albedo using model τ_{cld} and a simplified cloud albedo equation based upon a two-stream approximation and assumed asymmetry parameter of 0.85 ($\alpha^{cld} \approx \tau_{cld} / \tau_{cld} + 7.7$) [*Lacis and Hansen*, 1974]. Cloud albedo is calculated for every data point with τ_{cld} greater than 0.03 in the modeled cloud field, and these data are input to a simple TOA albedo model ($\alpha^{TOA} = R_{clr} + [(1 - R_{clr})^2 * (R_{cld} + R^*_{cld})/1 - R_{clf} * (R_{cld} + R^*_{cld})]$, where $R^*_{cld} = R_{sfc} * [(1 - R_{cld})^2/1-(R_{cld}*R_{sfc})]$, with assumed ocean surface albedo (R_{sfc}) of 0.05.

[c] CALIOP two-year cloud cover mean (standard deviation) of monthly values. N = 96 (24 months x 4 gridbox values).

[d] Cloud Optical depth threshold for CALIOP and HSRL is τ greater than 0.03 *(Chepfer, H., G. Cesana, D. Winker, B. Getzewich, and M. Vaughan, Comparison of two different cloud climatologies derived from CALIOP-Level 1 observations: the CALIPSO-ST and the CALIPSO-GOCCP, submitted to Journal of Atmospheric and Oceanic Technology, 2012).* and for MODIS is τ greater than 0.4 [*Ackerman et al*., 2008]. Optically-thin cloud is defined as a cloudy FOV where the number of photos required for surface detection (n) is greater than the minimum number (n_*) required i.e., $n/n_* > 1$.

[e] Highest resolution HSRL achieved given the HSRL PRF = 200 Hz and assuming aircraft velocity = 120 m s^{-1} (~1 m).

FIGURE CAPTIONS

Figure 1. Cumulative fraction of MODIS L3 liquid water cloud optical depth (τ_{cld}) for 12 months of ocean daytime data spanning ±45° latitude. Cloud albedo is approximated as (τ_{cld}/τ_{cld}+7.7) [*Lacis and Hansen*, 1974]. MODIS data suggest approximately one-third of low clouds over the oceans have optical depth less than 3 (optically-thin cloud definition, this study). In addition, such clouds may contribute up to 15% to total low-cloud albedo. Inset figure describes relative scales of CALIOP receiver footprint at single-shot resolution and MODIS pixel at cloud product resolution. It should be noted that at most, 3 CALIPSO footprints will traverse a given MODIS (on Aqua) pixel.

Figure 2. a) A bimodal distribution of 2 years of ocean nighttime lidar integrated attenuated backscatter signal at 532 nm (integrated from 0 to 3 km altitude), red dashed line is Rayleigh IABS from CALIOP molecular number density profile for a tropical Pacific transect. The modes represent clear and cloudy atmospheric regions, as classified by the CALIOP Vertical Feature Mask cloud-aerosol discrimination algorithm; b) marine low-cloud data suggests optically-thin cloud profiles (as defined in Section 2) populate not only the clear-cloud transition region, but also the broader marine low-cloud field.

Figure 3. a) A two-dimensional (5 km x 10 km), and, b) one-dimensional (10 km) view of a high-cloud-screened broken marine low-cloud scene, generated from CALIOP data along a 10 km daytime orbit segment over the northwest tropical Atlantic [32°N, 77°W] on 27 May 2007: a) Wide Field Camera (WFC) band-averaged radiance (620-670 nm) at 125 m horizontal resolution with CALIOP ground track position superimposed. The WFC data are continuous, along-track radiances. Symbols along the CALOP track indicate clear (yellow square), optically-thin cloud (white circle), and optically-thick cloud (black circle), b) Collocated WFC radiance (black) and Level 1 532 nm attenuated backscatter integrated from 0 to 20 km (IABS) (pink) for the same segment as in a). Symbols identifying clear profiles, and cloud profiles flagged as optically-thin or optically-thick are also indicated in b).

Figure 4. Number of data points comprising a) the primary dataset for this analysis, i.e., the high-cloud-screened non-polar ocean dataset, and b) the high-cloud-screened cloud length dataset Data for cloud length calculations are a subset of a), requiring a continuous transect at least 100 km in length. Data are 5°x5° resolution. Total number of data points: a) 1.4 x 10^8, b) 3.9 x 10^7.

Figure 5. Two-year mean ocean nighttime a) marine low-cloud cover, b) optically-thin marine low-cloud cover, and c) optically-thin fraction of marine low cloud (see Table 2 for fraction definitions). Data are 5°x5° resolution. Corresponding domain-averaged values are a) 0.50 (0.25), b) 0.23 (0.09), and c) 0.45 (0.28), mean (standard deviation). For this calculation gridbox values are weighted by the fraction of each gridbox that is ocean, and f_{thin_cld} *values are also weighted by* f_{cld}.

Figure 6. Joint distribution of monthly nighttime gridded optically-thin fraction of marine low cloud, as function of marine low-cloud cover, over-plotted with two-year mean gridbox values (grey). Both monthly and two-year averaged data exhibit a strong negative correlation. The correlation coefficient for the monthly data is -0.83, significant at the 95% confidence level.

Figure 7. Cloud length distribution based upon two years of gridded data for marine low cloud, "majority optically-thin" cloud, and "majority optically-thick" cloud. Each "Majority" category includes only clouds comprising greater than 90% cloud profiles belonging to either the optically-thin or optically-thick category. Size bins are logarithmically spaced and ordinate axis is normalized frequency. $\beta = 2$ line shown for reference. Inset: marine low-cloud length distribution for the following regions [region center latitude, longitude]: California stratocumulus region (Sc) [25°N, 125°W], tropical Pacific stratocumulus to cumulus transition (Sc-Cu Trans) [15°N, 135°W], and tropical Pacific trade wind cumulus (Cu) [15°S, 155°W]. Abscissa values are cloud length bin centers.

Figure 8. Cloud length at median cloud cover (L_{50}) for a) marine low cloud, b) "majority optically-thin" cloud, c) "majority optically-thick" cloud, from two years of ocean nighttime data at 5°x5° resolution. Low (high) cloud cover values are dominated by small (large) clouds. "Majority optically-thin" clouds dominate the cloud type in regions of low cloud cover, e.g. trade wind cumulus regions. Each "majority" category includes only clouds comprising greater than 90% cloud profiles belonging to either the optically-thin or optically-thick category. White over ocean regions in c) indicates that no "majority optically-thick" clouds observed.

Figure 9. HSRL (black) and CALIOP (pink) marine low-cloud length distributions with bootstrap derived 95% confidence intervals [*Efron and Gong,* 1983]. Dashed line is $\beta = 2$, shown for reference. Where cloud size bins overlap, HSRL samples fewer clouds than CALIOP can resolve. HSRL samples more clouds at smaller sizes than CALIOP. Sub-sampling HSRL (blue stars) produces good agreement between HSRL and CALIOP size distributions. CALIOP and HSRL mean f_{cld} values agree to within 2 standard deviations. However, mean $f_{thin,cld}$ values do not agree, with HSRL $f_{thin,cld}$ lower than CALIOP $f_{thin,cld}$. Inset schematic describes suggested mechanism for $f_{thin,cld}$ discrepancy, i.e., it is the result of differences in instrument sampling methods: blue circles represent CALIOP 90 m FOVs, and orange bar shows the relative size of the HSRL FOV compared to the CALIOP FOV.

Figure 10. Optically-thin fraction of marine low-cloud length for non-polar oceans, and three regions with different dominant cloud types [region center latitude, longitude]: California stratocumulus region (Sc) [25°N, 125°W], tropical Pacific stratocumulus to cumulus transition (Sc-Cu Trans) [15°N, 135°W], and tropical Pacific trade wind cumulus (Cu) [15°S, 155°W]. Increasing optically-thin fraction as cloud length decreases is observed across all regions, despite different cloud types. Vertical bars are 95% confidence intervals calculated from the bootstrap method [*Efron and Gong,* 1983]. Abscissa values are cloud length bin centers.

Figure 11. Vertical distribution of two-year mean optically-thick (red) and optically-thin (black) cloud top height (top row) and, optically-thin cloud base height (bottom row) for 3

cloud regimes [region center latitude, longitude]: a) and d) California stratocumulus region (Sc) [25°N, 125°W], b) and e) tropical Pacific stratocumulus to cumulus transition (Sc-Cu Trans) [15°N, 135°W], and c) and f) tropical Pacific trade wind cumulus (Cu) [15°S, 155°W]. Layer boundaries are identified by CALIPSO feature detection algorithm at full horizontal resolution, and 60m vertical resolution.

Figure 12. Normalized density distributions of optically-thin cloud top height and layer depth for 3 cloud types [region center latitude, longitude]: a) California stratocumulus region [25°N, 125°W], b) tropical Pacific stratocumulus to cumulus transition (Sc-Cu Trans) [15°N, 135°W], and c) tropical Pacific trade wind cumulus (Cu) [15°S, 155°W]. Inset figures are layer depth distributions for each region, overlaid with a gamma distribution (red). Text is region mean (standard deviation) layer depth (km), and number of full-resolution optically-thin cloud profiles for each region. Layer depth histogram is normalized such that the area under the curve = 1.

Figure 13. An aerial photograph of a typical trade wind cumulus cloud field observed in the Western Caribbean during the Rain in Cumulus over Ocean (RICO) field program. Apparent is the wide range of cloud depths and horizontal extents. (Image courtesy of B. Stevens).

Figure 14. Two years of CALIOP tropical Pacific trade wind region observations (black dots) ± 95% confidence intervals from bootstrap method [*Efron and Gong,* 1983], and cascade model output simulating this cloud regime, sampled with CALIOP FOV (black circles), MODIS FOV (red circles), HSRL FOV (blue circles), and HSRL Full Res i.e., highest resolution sampling of model output (blue squares). Size bins are logarithmically spaced and ordinate axis is normalized frequency. $\beta = 2$ line (dashed line) shown for reference. Cascade model output from 100 runs with $H = 0.07$ and $p = 0.0005$. Abscissa values are cloud length bin centers.

Figure 15 Cloudy fields of view (FOVs) and partially cloud-filled FOVs (pFOVs) values binned by cloud length, as estimated from model simulated optical depth (τ) values sampled at CALIOP FOV resolution. Displayed for each cloud length bin is the fraction of all cloud FOVs that are less than 100% cloudy, i.e., pFOV (filled circles); the median cloud fraction for pFOVs (filled squares); the fraction of optically-thin pFOVs incorrectly classified as optically-thin, i.e., a FOV with mean n/n_* and mean τ of the cloudy-only segment greater than 3 (filled diamonds). Cascade model output is from 100 runs with H = 0.07 and p = 0.0005.

FIGURES

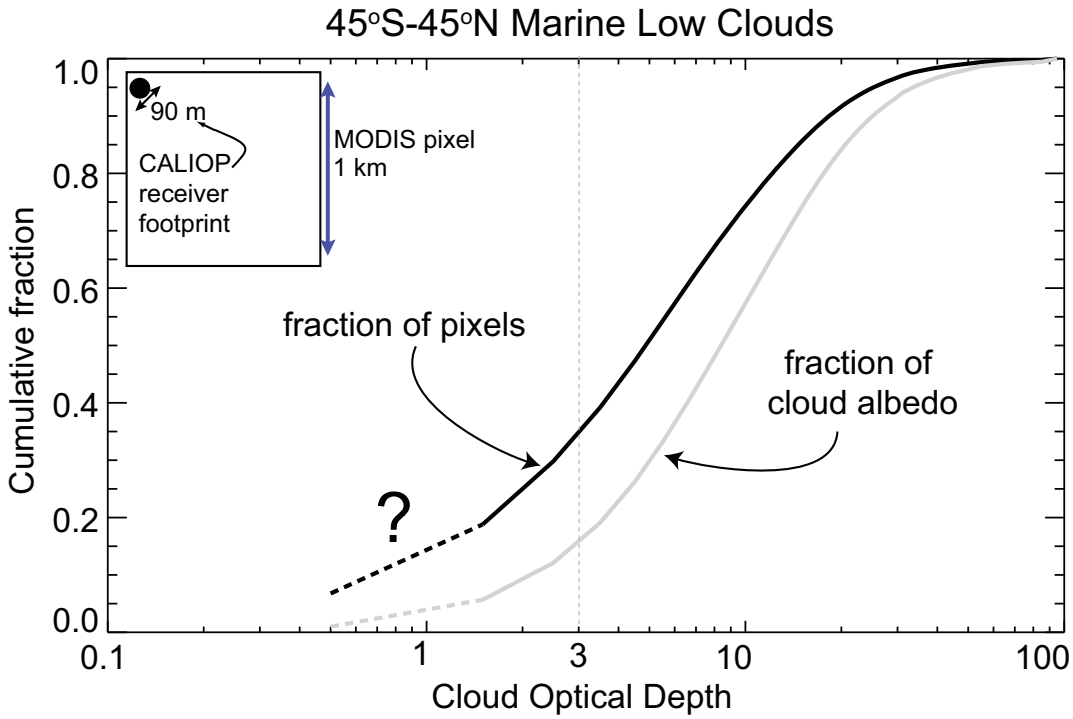

Figure 1. Cumulative fraction of MODIS L3 liquid water cloud optical depth (τ_{cld}) for 12 months of ocean daytime data spanning ±45° latitude. Cloud albedo is approximated as (τ_{cld}/τ_{cld}+7.7) [*Lacis and Hansen*, 1974]. MODIS data suggest approximately one-third of low clouds over the oceans have optical depth less than 3 (optically-thin cloud definition, this study). In addition, such clouds may contribute up to 15% to total low-cloud albedo. Inset figure describes relative scales of CALIOP receiver footprint at single-shot resolution and MODIS pixel at cloud product resolution. It should be noted that at most, 3 CALIPSO footprints will traverse a given MODIS (on Aqua) pixel.

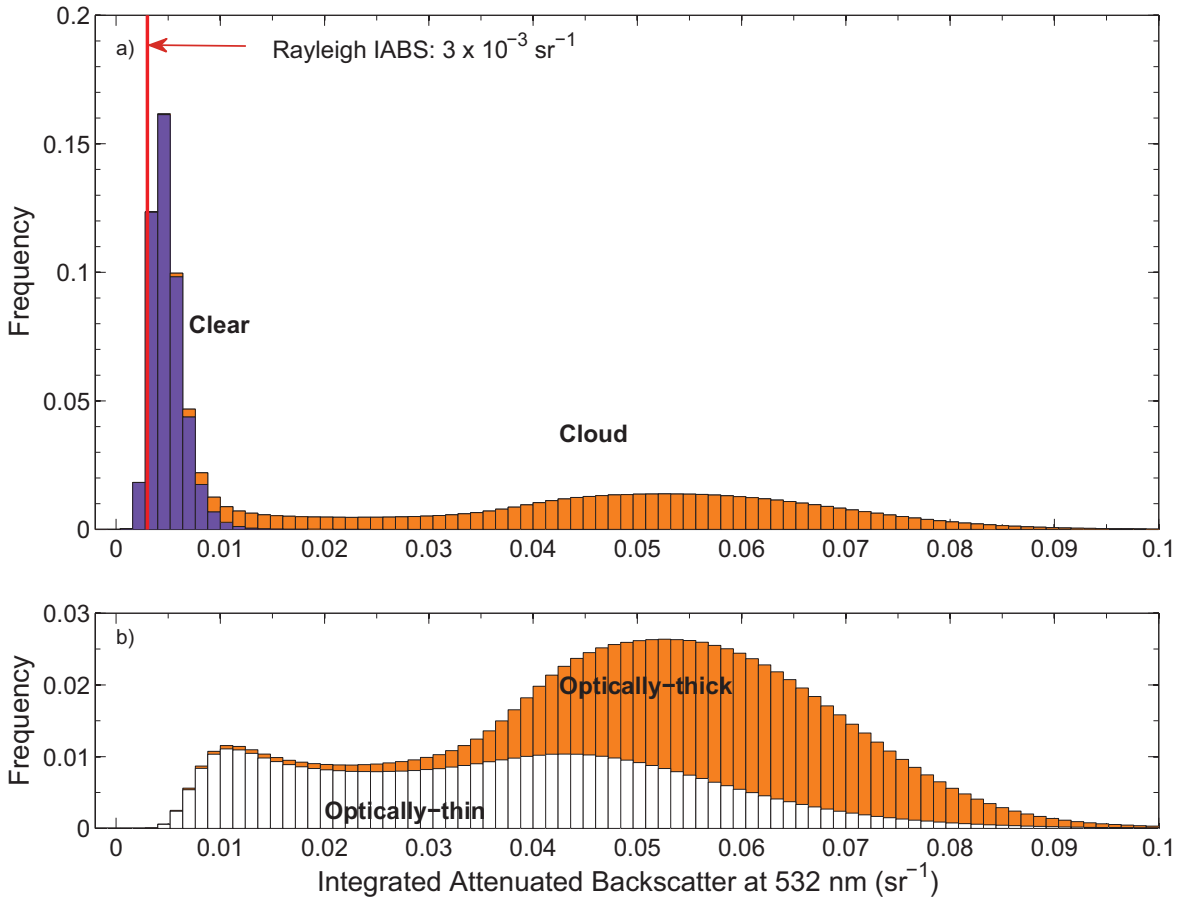

Figure 2. a) A bimodal distribution of 2 years of ocean nighttime lidar integrated attenuated backscatter signal at 532 nm (integrated from 0 to 3 km altitude), red dashed line is Rayleigh IABS from CALIOP molecular number density profile for a tropical Pacific transect. The modes represent clear and cloudy atmospheric regions, as classified by the CALIOP Vertical Feature Mask cloud-aerosol discrimination algorithm; b) marine low-cloud data suggests optically-thin cloud profiles (as defined in Section 2) populate not only the clear-cloud transition region, but also the broader marine low-cloud field.

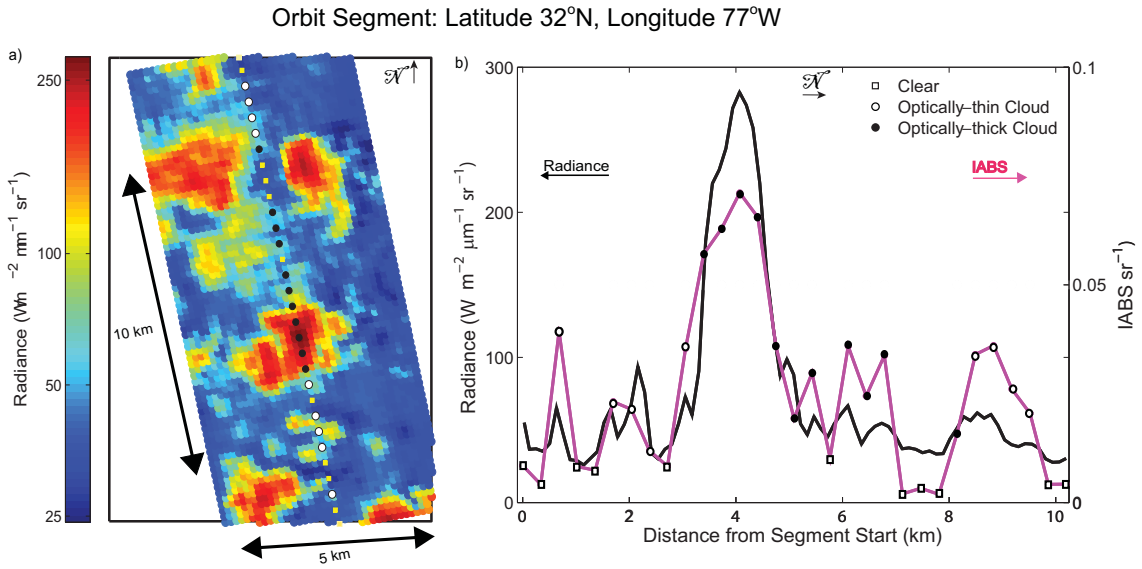

Figure 3. a) A two-dimensional (5 km x 10 km), and, b) one-dimensional (10 km) view of a high-cloud-screened broken marine low-cloud scene, generated from CALIOP data along a 10 km daytime orbit segment over the northwest tropical Atlantic [32°N, 77°W] on 27 May 2007: a) Wide Field Camera (WFC) band-averaged radiance (620-670 nm) at 125 m horizontal resolution with CALIOP ground track position superimposed. The WFC data are continuous, along-track radiances. Symbols along the CALOP track indicate clear (yellow square), optically-thin cloud (white circle), and optically-thick cloud (black circle), b) Collocated WFC radiance (black) and Level 1 532 nm attenuated backscatter integrated from 0 to 20 km (IABS) (pink) for the same segment as in a). Symbols identifying clear profiles, and cloud profiles flagged as optically-thin or optically-thick are also indicated in b).

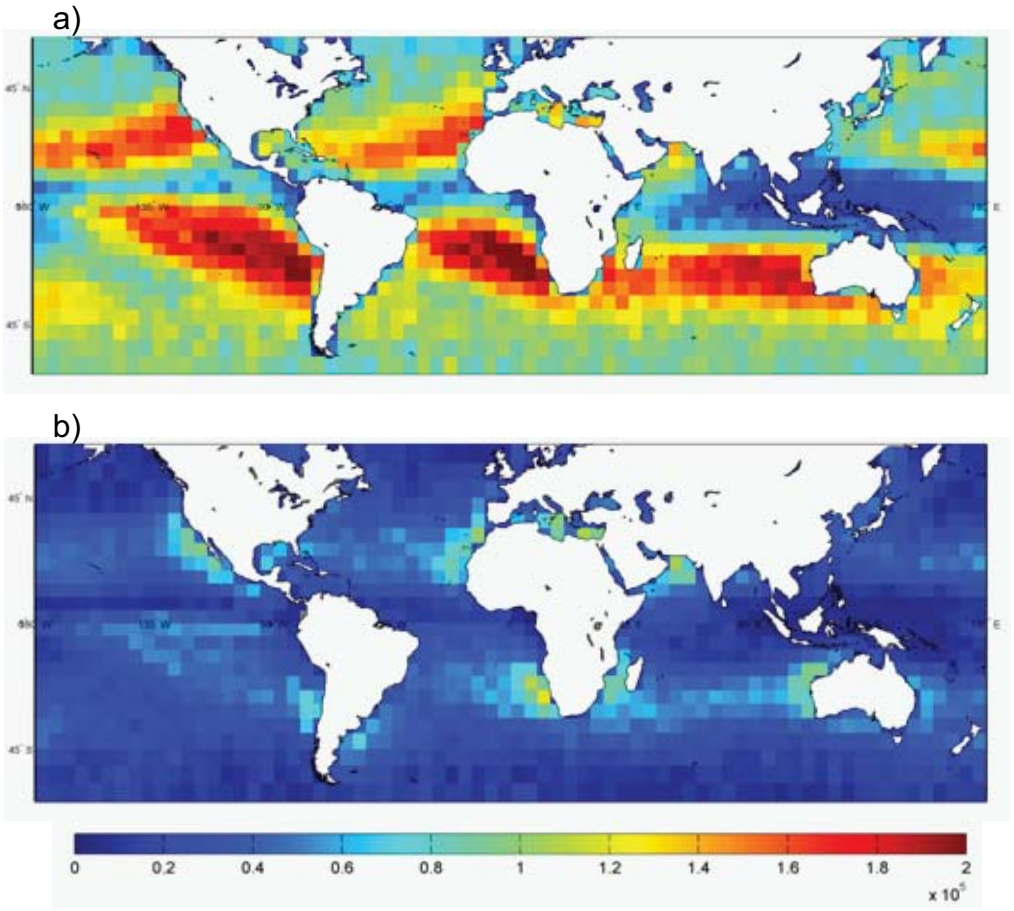

Figure 4. Number of data points comprising a) the primary dataset for this analysis, i.e., the high-cloud-screened non-polar ocean dataset, and b) the high-cloud-screened cloud length dataset Data for cloud length calculations are a subset of a), requiring a continuous transect at least 100 km in length. Data are 5°x5° resolution. Total number of data points: a) 1.4 x 10^8, b) 3.9 x 10^7.

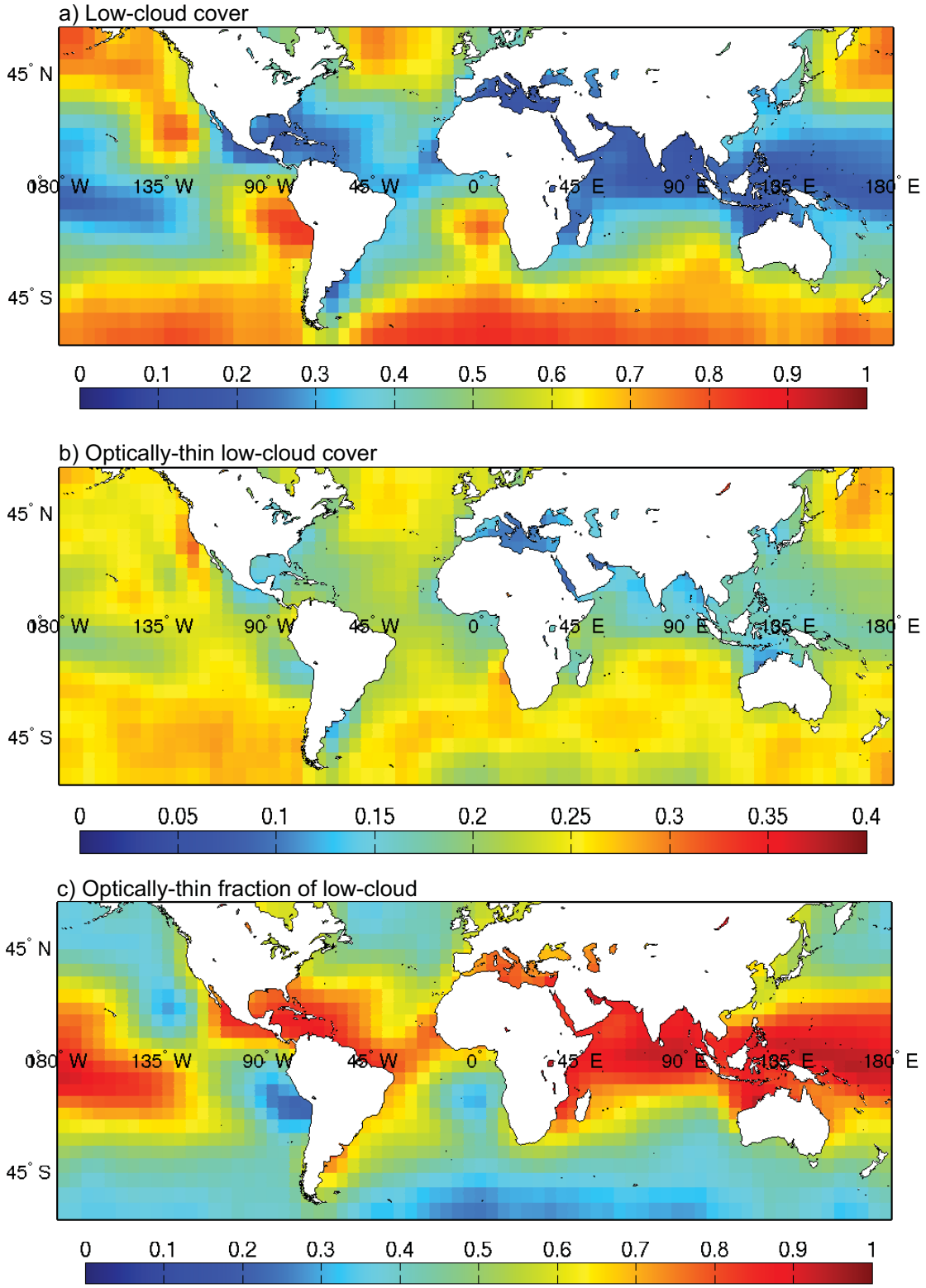
a) Low-cloud cover
45° N
0
180° W
135° W
90° W
45° W
0
45° E
90° E
135° E
180° E
45° S
0 0.1 0.2 0.3 0.4 0.5 0.6 0.7 0.8 0.9 1
b) Optically-thin low-cloud cover
45° N
0
180° W
135° W
90° W
45° W
0
45° E
90° E
135° E
180° E
45° S
0 0.05 0.1 0.15 0.2 0.25 0.3 0.35 0.4
c) Optically-thin fraction of low-cloud
45° N
0
180° W
135° W
90° W
45° W
0
45° E
90° E
135° E
180° E
45° S
0 0.1 0.2 0.3 0.4 0.5 0.6 0.7 0.8 0.9 1

1283

Figure 5. Two-year mean ocean nighttime a) marine low-cloud cover, b) optically-thin marine low-cloud cover, and c) optically-thin fraction of marine low cloud (see Table 2 for fraction definitions). Data are 5°x5° resolution. Corresponding domain-averaged values are a) 0.50 (0.25), b) 0.23 (0.09), and c) 0.45 (0.28), mean (standard deviation). For this calculation gridbox values are weighted by the fraction of each gridbox that is ocean, and f_{thin_cld} *values are also weighted by* f_{cld}.

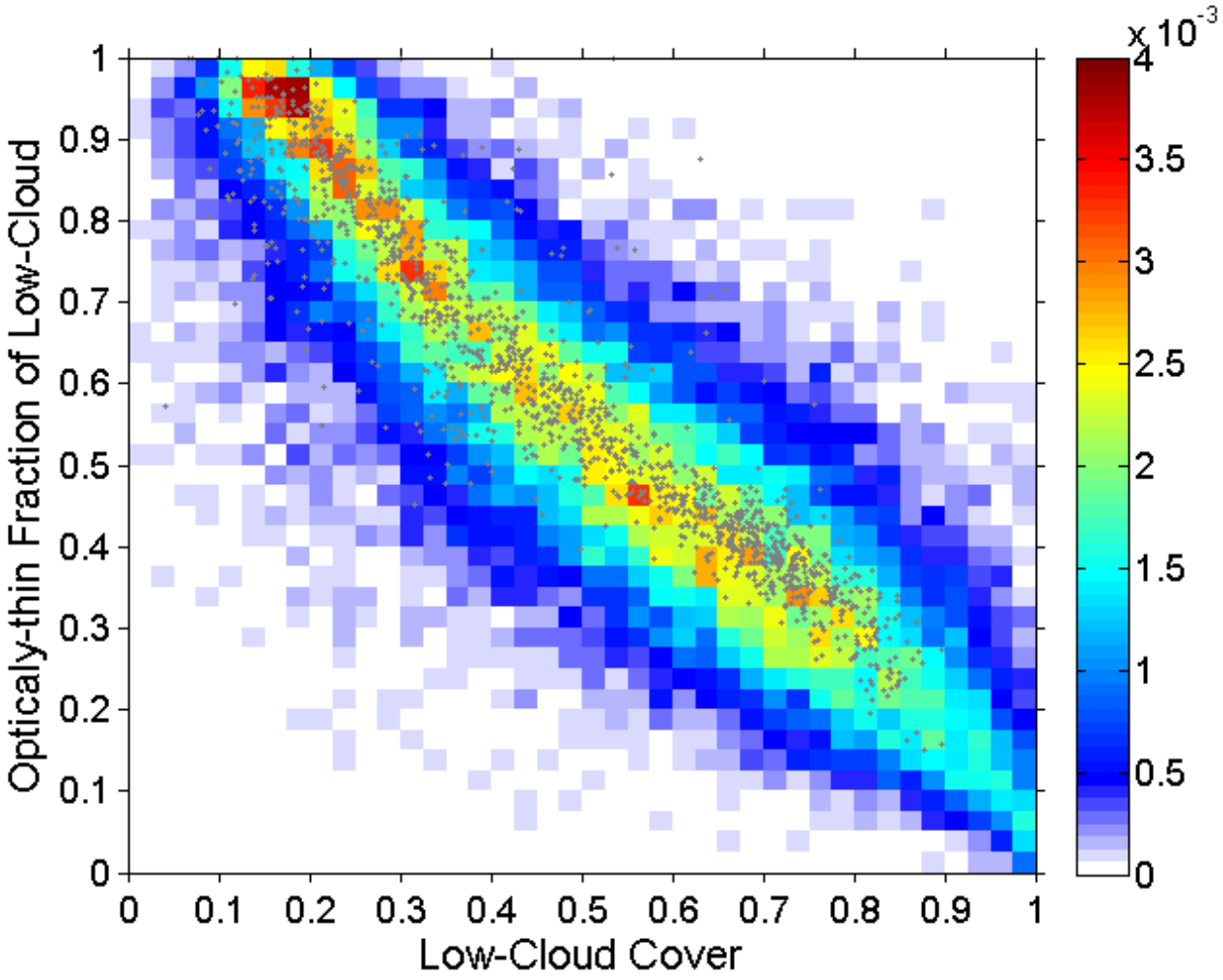

Figure 6. Joint distribution of monthly nighttime gridded optically-thin fraction of marine low cloud, as function of marine low-cloud cover, over-plotted with two-year mean gridbox values (grey). Both monthly and two-year averaged data exhibit a strong negative correlation. The correlation coefficient for the monthly data is -0.83, significant at the 95% confidence level.

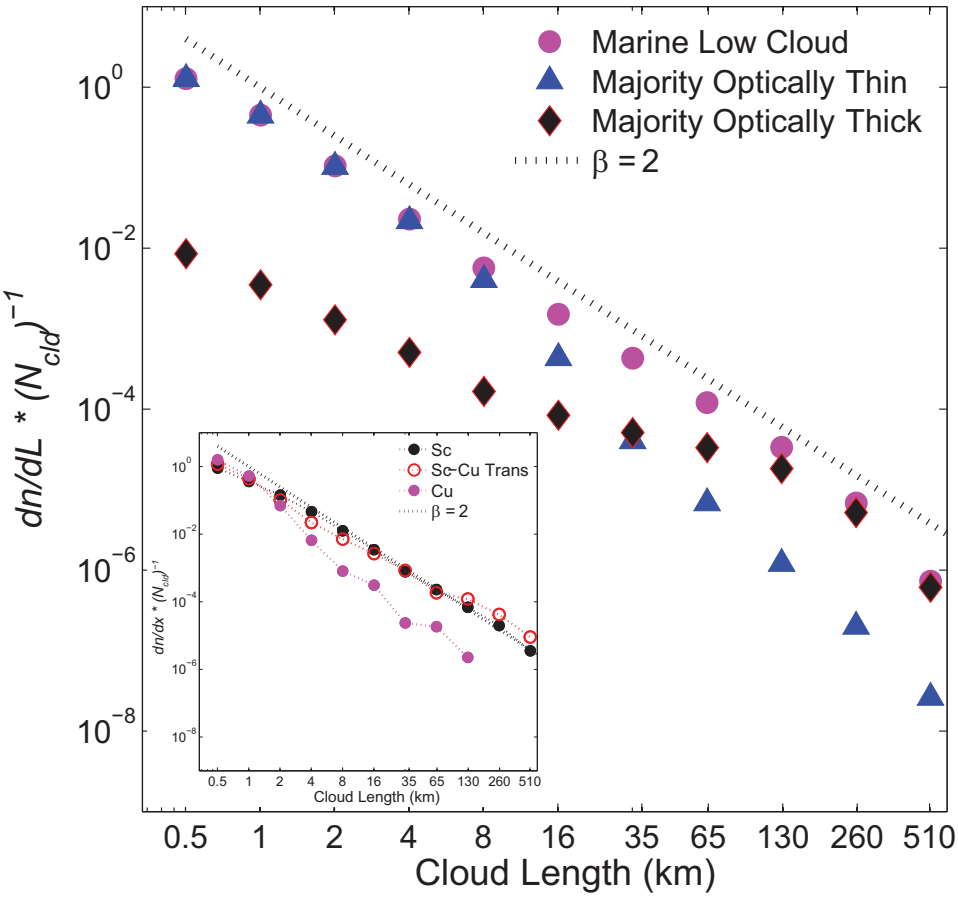

Figure 7. Cloud length distribution based upon two years of gridded data for marine low cloud, "majority optically-thin" cloud, and "majority optically-thick" cloud. Each "Majority" category includes only clouds comprising greater than 90% cloud profiles belonging to either the optically-thin or optically-thick category. Size bins are logarithmically spaced and ordinate axis is normalized frequency. $\beta = 2$ line shown for reference. Inset: marine low-cloud length distribution for the following regions [region center latitude, longitude]: California stratocumulus region (Sc) [25°N, 125°W], tropical Pacific stratocumulus to cumulus transition (Sc-Cu Trans) [15°N, 135°W], and tropical Pacific trade wind cumulus (Cu) [15°S, 155°W]. Abscissa values are cloud length bin centers.

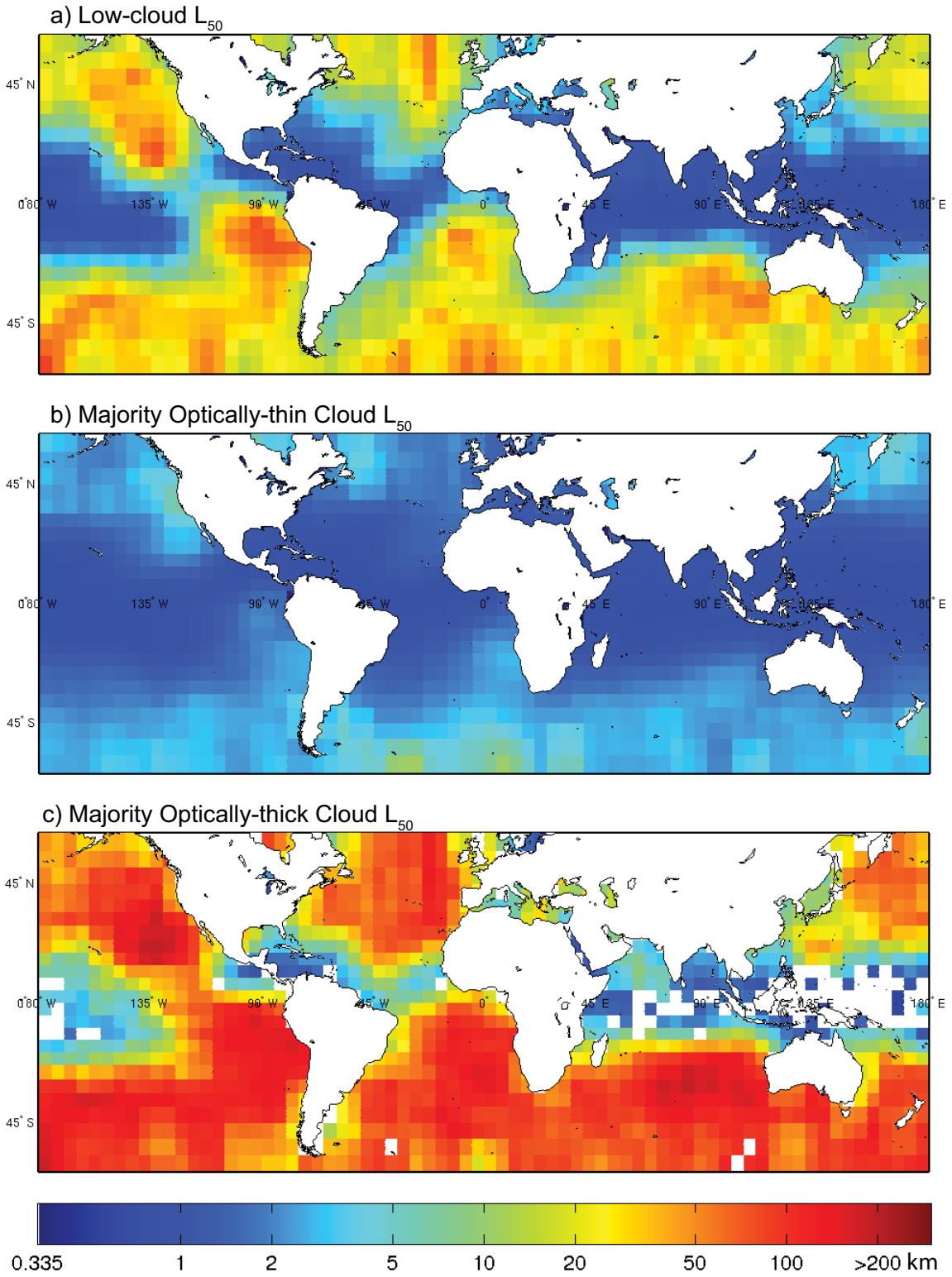

Figure 8. Cloud length at median cloud cover (L_{50}) for a) marine low cloud, b) "majority optically-thin" cloud, c) "majority optically-thick" cloud, from two years of ocean nighttime data at 5°x5° resolution. Low (high) cloud cover values are dominated by small (large) clouds. "Majority optically-thin" clouds dominate the cloud type in regions of low cloud cover, e.g. trade wind cumulus regions. Each "majority" category includes only clouds

1314 comprising greater than 90% cloud profiles belonging to either the optically-thin or
1315 optically-thick category. White over ocean regions in c) indicates that no "majority
1316 optically-thick" clouds observed.

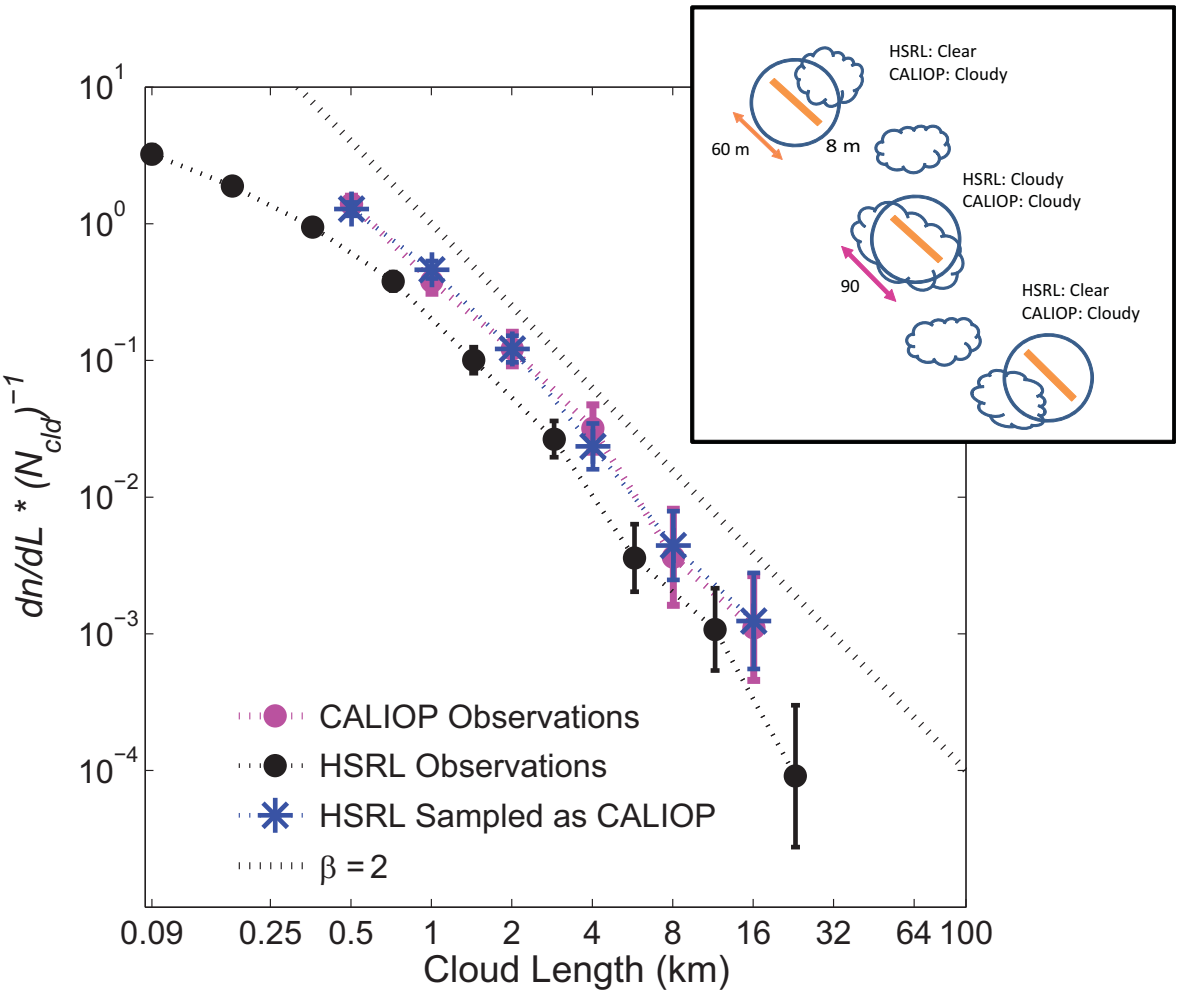

Figure 9. HSRL (black) and CALIOP (pink) marine low-cloud length distributions with bootstrap derived 95% confidence intervals [*Efron and Gong,* 1983]. Dashed line is $\beta = 2$, shown for reference. Where cloud size bins overlap, HSRL samples fewer clouds than CALIOP can resolve. HSRL samples more clouds at smaller sizes than CALIOP. Sub-sampling HSRL (blue stars) produces good agreement between HSRL and CALIOP size distributions. CALIOP and HSRL mean f_{cld} values agree to within 2 standard deviations. However, mean $f_{thin,cld}$ values do not agree, with HSRL $f_{thin,cld}$ lower than CALIOP $f_{thin,cld}$. Inset schematic describes suggested mechanism for $f_{thin,cld}$ discrepancy, i.e., it is the result of differences in instrument sampling methods: blue circles represent CALIOP 90 m FOVs, and orange bar shows the relative size of the HSRL FOV compared to the CALIOP FOV.

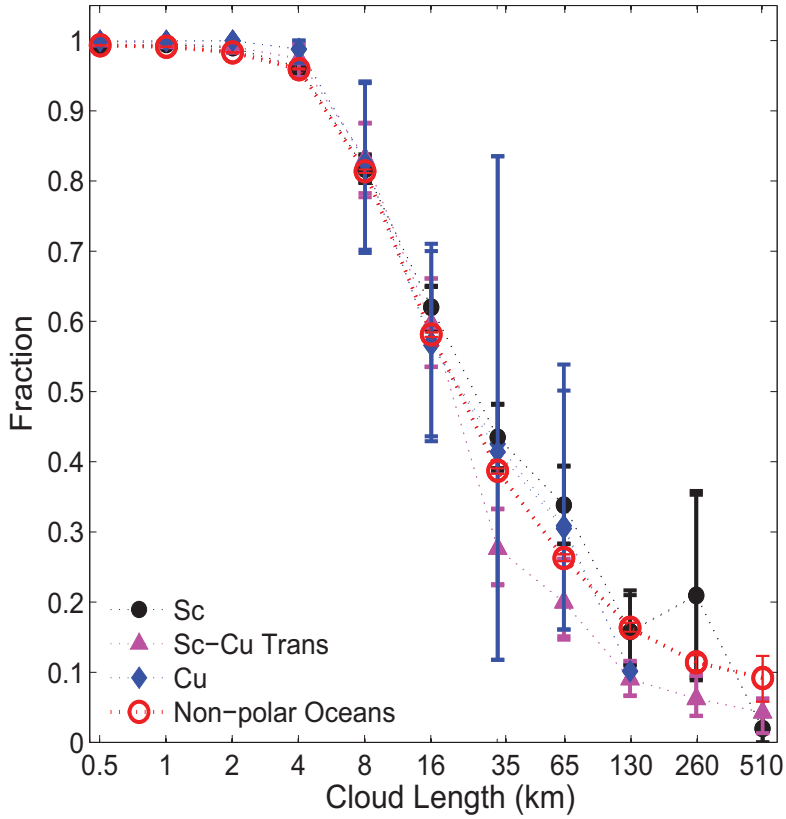

Figure 10. Optically-thin fraction of marine low-cloud length for non-polar oceans, and three regions with different dominant cloud types [region center latitude, longitude]: California stratocumulus region (Sc) [25°N, 125°W], tropical Pacific stratocumulus to cumulus transition (Sc-Cu Trans) [15°N, 135°W], and tropical Pacific trade wind cumulus (Cu) [15°S, 155°W]. Increasing optically-thin fraction as cloud length decreases is observed across all regions, despite different cloud types. Vertical bars are 95% confidence intervals calculated from the bootstrap method [*Efron and Gong,* 1983]. Abscissa values are cloud length bin center.

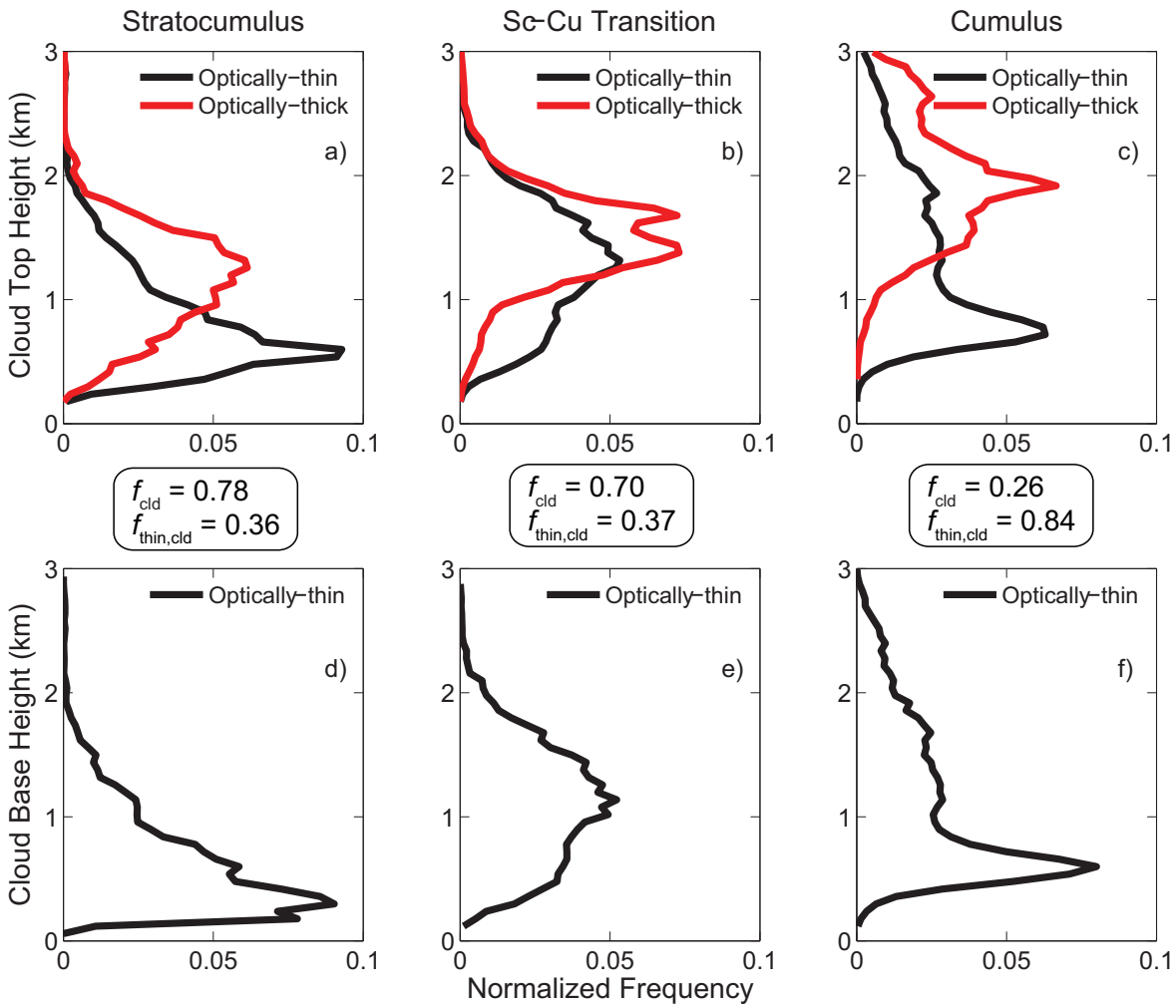

Figure 11. Vertical distribution of two-year mean optically-thick (red) and optically-thin (black) cloud top height (top row) and, optically-thin cloud base height (bottom row) for 3 cloud regimes [region center latitude, longitude]: a) and d) California stratocumulus region (Sc) [25°N, 125°W], b) and e) tropical Pacific stratocumulus to cumulus transition (Sc-Cu Trans) [15°N, 135°W], and c) and f) tropical Pacific trade wind cumulus (Cu) [15°S, 155°W]. Layer boundaries are identified by CALIPSO feature detection algorithm at full horizontal resolution, and 60m vertical resolution.

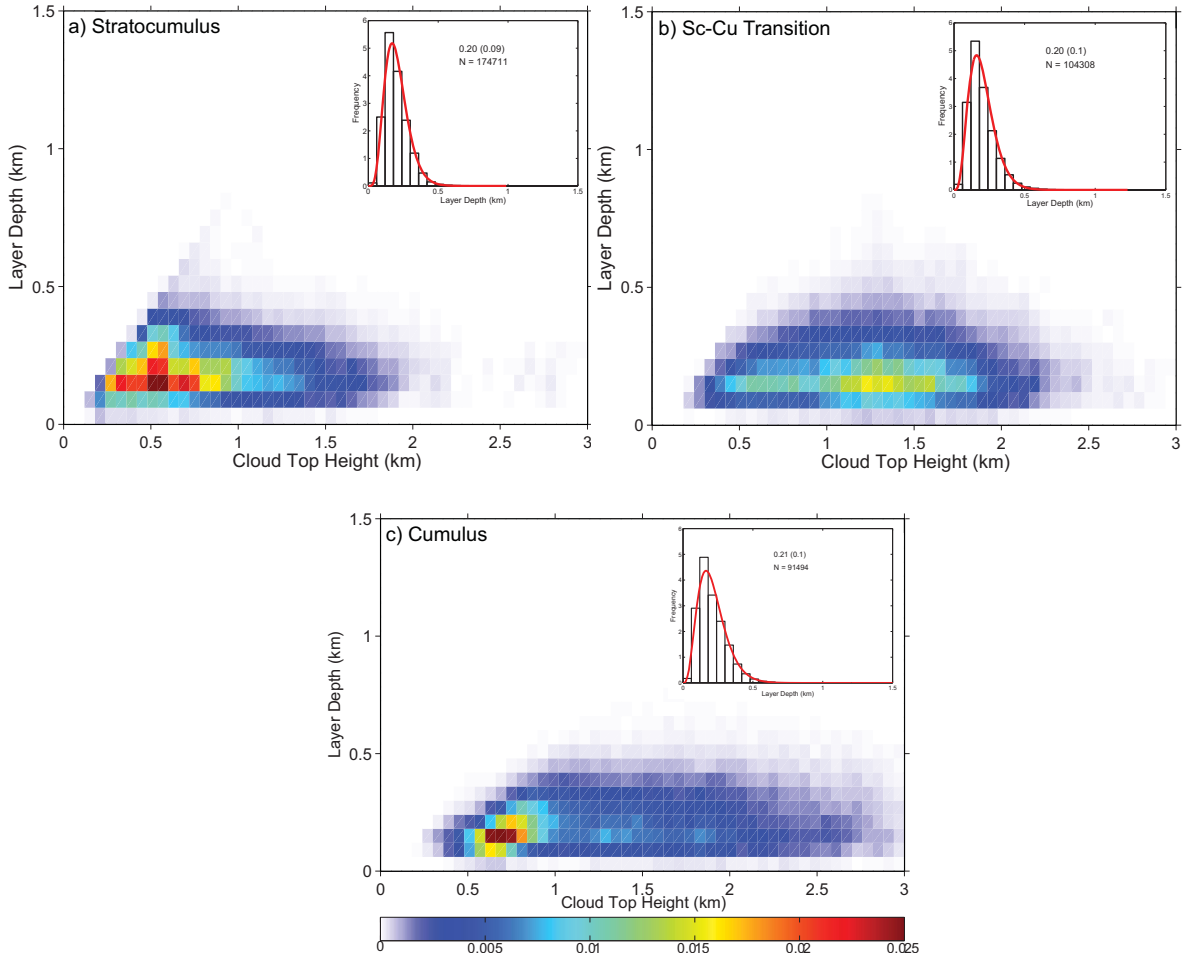

Figure 12. Normalized density distributions of optically-thin cloud top height and layer depth for 3 cloud types [region center latitude, longitude]: a) California stratocumulus region [25°N, 125°W], b) tropical Pacific stratocumulus to cumulus transition (Sc-Cu Trans) [15°N, 135°W], and c) tropical Pacific trade wind cumulus (Cu) [15°S, 155°W]. Inset figures are layer depth distributions for each region, overlaid with a gamma distribution (red). Text is region mean (standard deviation) layer depth (km), and number of full-resolution optically-thin cloud profiles for each region. Layer depth histogram is normalized such that the area under the curve = 1.

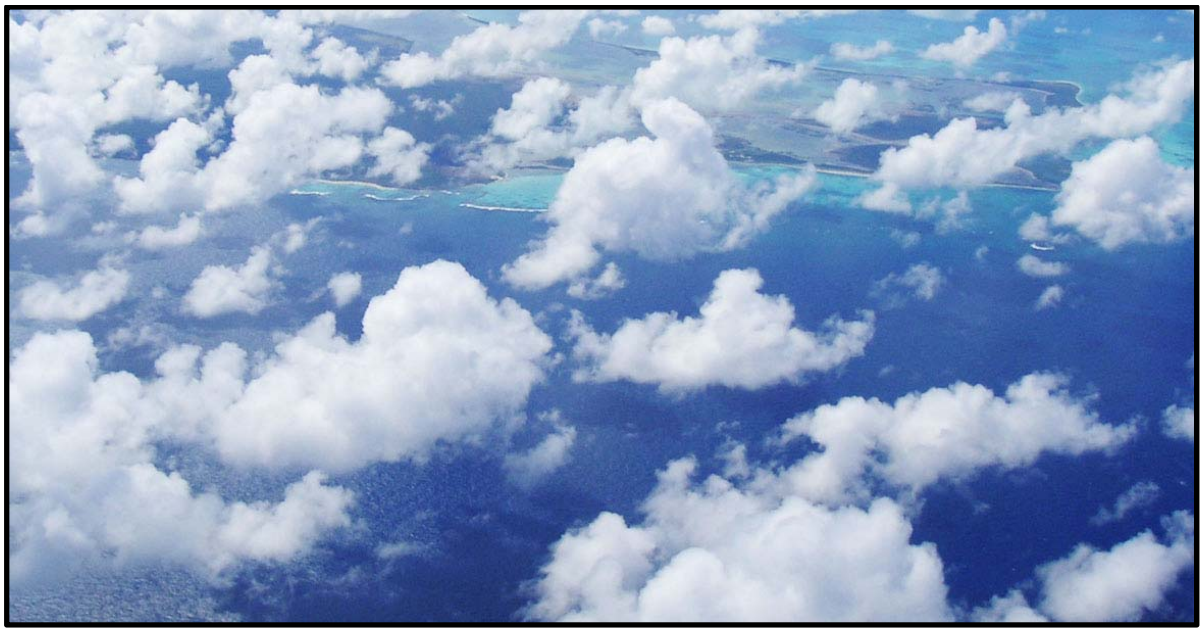

Figure 13. An aerial photograph of a typical trade wind cumulus cloud field observed in the Western Caribbean during the Rain in Cumulus over Ocean (RICO) field program. Apparent is the wide range of cloud depths and horizontal extents. (Image courtesy of B. Stevens).

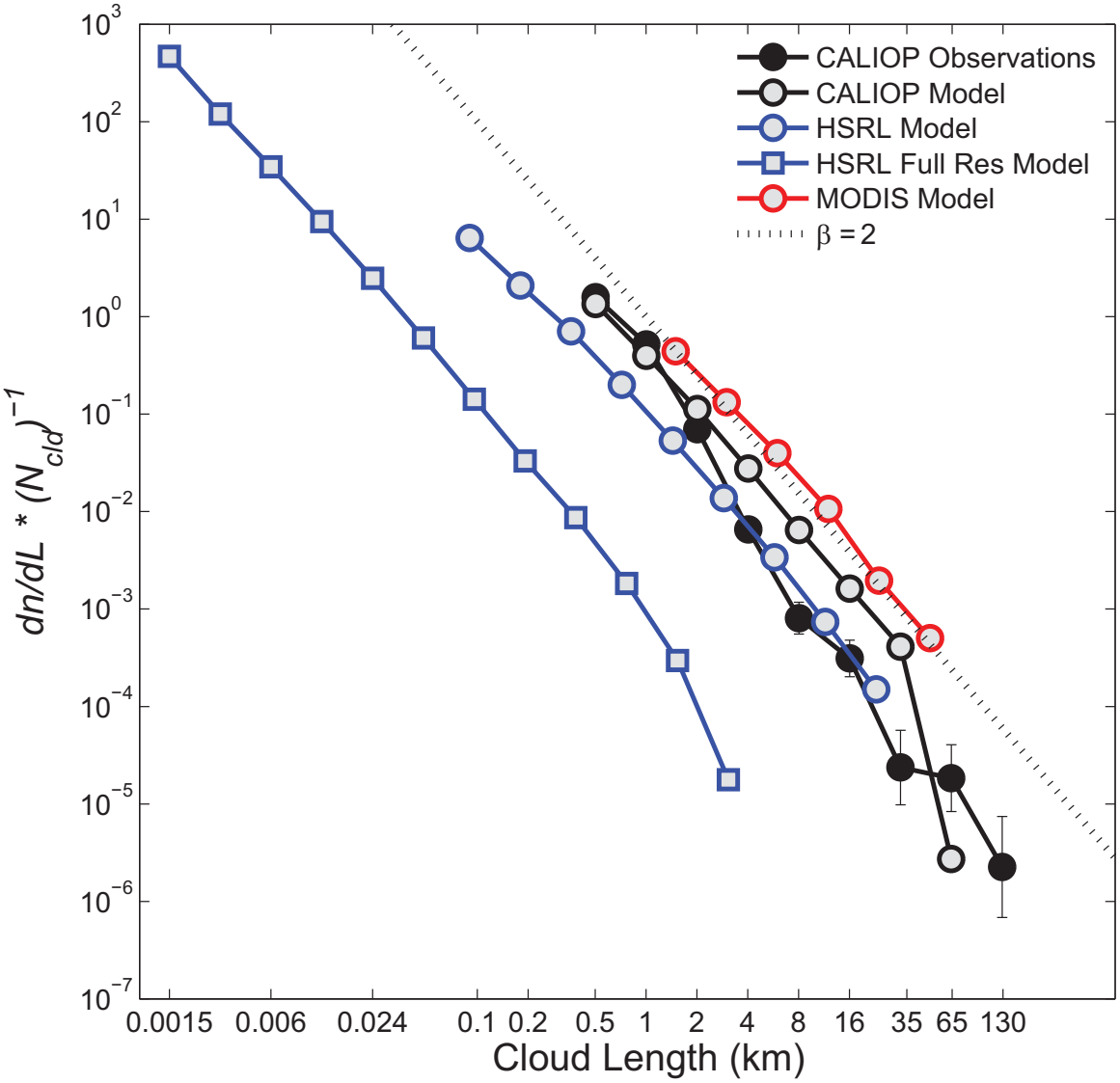

Figure 14. Two years of CALIOP tropical Pacific trade wind region observations (black dots) ± 95% confidence intervals from bootstrap method [*Efron and Gong,* 1983], and cascade model output simulating this cloud regime, sampled with CALIOP FOV (black circles), MODIS FOV (red circles), HSRL FOV (blue circles), and HSRL Full Res i.e., highest resolution sampling of model output (blue squares). Size bins are logarithmically spaced and ordinate axis is normalized frequency. β = 2 line (dashed line) shown for reference. Cascade model output from 100 runs with H = 0.015 and p = 0.05. Abscissa values are cloud length bin center.

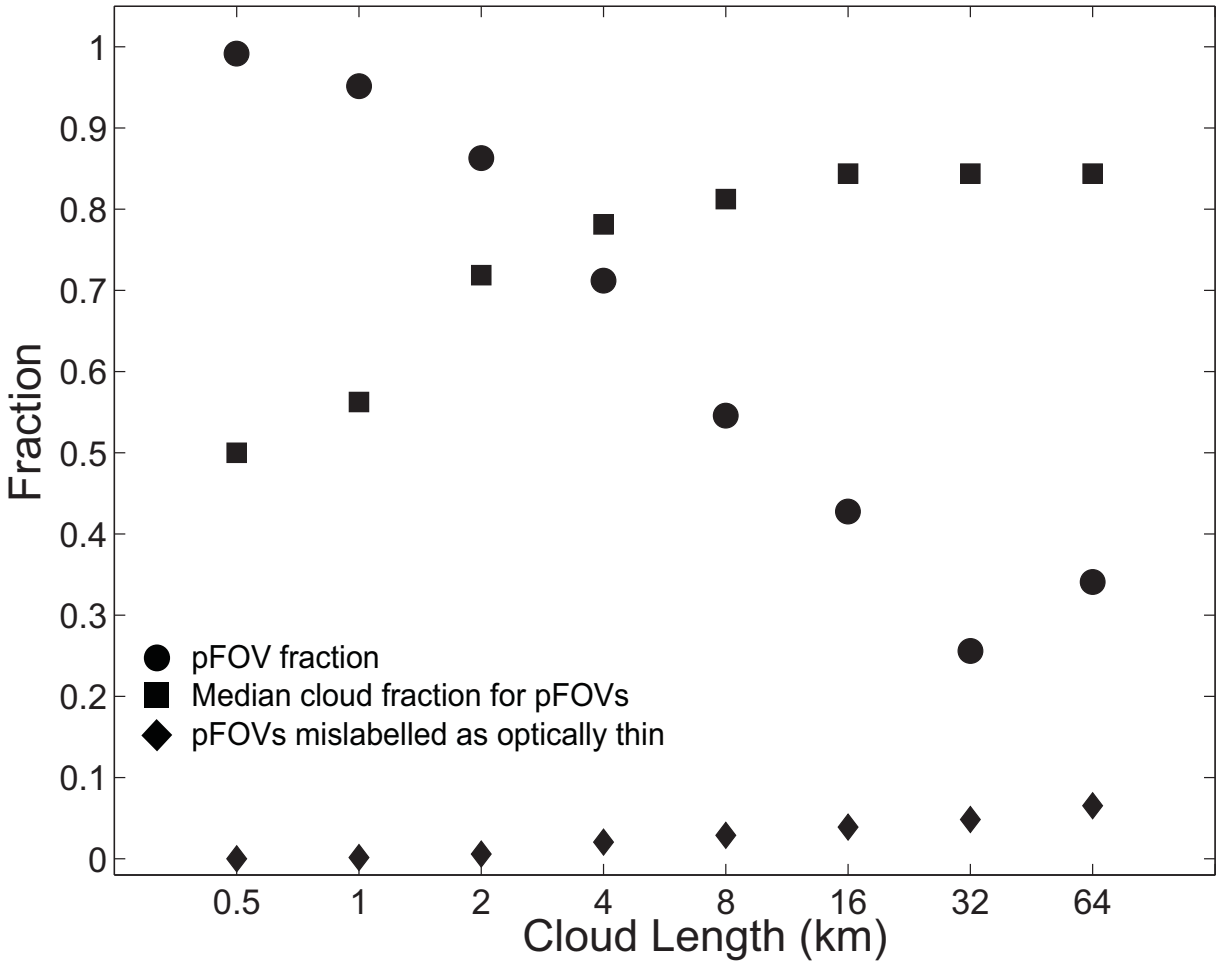

Figure 15 Cloudy fields of view (FOVs) and partially cloud-filled FOVs (pFOVs) values binned by cloud length, as estimated from model simulated optical depth (τ) values sampled at CALIOP FOV resolution. Displayed for each cloud length bin is the fraction of all cloud FOVs that are less than 100% cloudy, i.e., pFOV (filled circles); the median cloud fraction for pFOVs (filled squares); the fraction of optically-thin pFOVs incorrectly classified as optically-thin, i.e., a FOV with mean n/n_* and mean τ of the cloudy-only segment greater than 3 (filled diamonds). Cascade model output is from 100 runs with H = 0.07 and p = 0.0005.